R. & M. No. 3257

MINISTRY OF AVIATION

AERONAUTICAL RESEARCH COUNCIL
REPORTS AND MEMORANDA

Measurements of the Direct Pitching-Moment Derivatives for Two-Dimensional Flow at Subsonic and Supersonic Speeds and for a Wing of Aspect Ratio 4 at Subsonic Speeds

By J. B. BRATT, B.A., B.Sc., W. G. RAYMER, B.Sc. (Eng.)
and J. E. G. TOWNSEND

OF THE AERODYNAMICS DIVISION, N.P.L.

LONDON: HER MAJESTY'S STATIONERY OFFICE
1962
PRICE £1 2s. 6d. NET

Measurements of the Direct Pitching-Moment Derivatives for Two-Dimensional Flow at Subsonic and Supersonic Speeds and for a Wing of Aspect Ratio 4 at Subsonic Speeds

By J. B. Bratt, B.A., B.Sc., W. G. Raymer, B.Sc. (Eng.) and J. E. G. Townsend

of the Aerodynamics Division, N.P.L.

*Reports and Memoranda No. 3257**

January, 1959

Summary. Apparatus based on a self-excitation technique has been developed for the measurement of direct pitching-moment derivatives at high speeds, and has proved to function satisfactorily.

Measurements have been made at subsonic speeds on a two-dimensional RAE 104 aerofoil, both with and without spoilers, and on a rectangular wing of aspect ratio 4 with the same section; and at supersonic speeds ($M = 1{\cdot}42$ and $1{\cdot}61$) on two-dimensional biconvex aerofoils of $7\frac{1}{2}$ per cent and 5 per cent thickness.

Comparisons with theory are made and discussed.

1. *Introduction.* An account is given in this paper of oscillatory tests carried out in the N.P.L. $9\frac{1}{2}$ in. square High Speed Tunnel. The main purpose in designing these tests was to obtain further information on the direct two-dimensional pitching-moment derivatives, both at subsonic and supersonic speeds; at the same time, however, the choice of a self-excitation technique enabled valuable experience to be gained in the application of this method to the measurement of these derivatives at high speeds.

Earlier high-speed measurements[1] at N.P.L. had employed a decaying oscillation technique and were limited to very low values of the frequency parameter ($0{\cdot}016$ at $M = 0{\cdot}9$) as a result of the high wind speeds involved. The attainment of higher values of the frequency parameter requires still greater frequencies of oscillation, which in practice leads to difficulty in the measurement of the stiffness derivative by the method of decaying oscillations, since the aerodynamic stiffness tends to become very small compared with the elastic stiffness. The resulting small change in frequency due to wind loading, from which the derivative is determined, cannot easily be measured with sufficient accuracy from the limited number of cycles frequently available. This difficulty is overcome by employing a self-excitation technique in which damping moments are automatically

* Previously issued as A.R.C. 20,714. Published with the permission of the Director, National Physical Laboratory.

balanced by an electromechanical feedback system to give a sustained oscillation which may be allowed to continue for a sufficient length of time to give the required accuracy. The damping moment is equal and opposite to the applied moment, and this is most conveniently determined from a measurement of the electrical driving power. The technique possesses considerable advantages at high speeds and high frequencies when compared with other steady oscillation methods designed to measure overall force, since these all require the balancing out of inertial reactions which are in general large compared with the aerodynamic reactions to be measured.

Although the apparatus described below was designed for two-dimensional tests, it was found possible to utilize one half of the system for measurements with finite aspect-ratio models by employing a half-model technique. Some results for a rectangular wing of aspect ratio 4 obtained by this method are included in the Report.

2. *Experimental Technique.* 2.1. *Mechanical System.* The general arrangement of the apparatus in relation to the tunnel working section is illustrated in Fig. 1. The tunnel is of the induced flow type with a vertical working section $9\frac{1}{2}$ in. square. Two identical vibratory systems were mounted on opposite sides of the tunnel with their axes coincident with that of the model. Each vibratory system consisted of a rigid steel spindle supported by two crossed-spring bearings which permitted axial rotation but were very stiff for lateral displacements. This provided built-in end conditions for the model, which was clamped to the spindles, and thus maintained a high value of flexural stiffness. Torsion bars connected between the spindles and earthed brackets provided elastic stiffness and determined the natural frequency of the system, which could be varied in discrete steps over a range of frequency by means of a graded set of torsion bars.

Each vibratory system was housed in an airtight box to prevent air flowing into the working section through the holes in the tunnel walls where the model was clamped to the spindles. One of the systems was mounted on a floating platform supported on vertical flexures in such a manner as to relieve axial stresses in the spring bearings due to distortion of the apparatus resulting from changes in temperature and internal pressure.

2.2. *Electromechanical Excitation.* The system was oscillated by means of four electromagnetic exciters of the pot-magnet type, the moving coils of which were fixed to the ends of rigid arms attached to the spindles. All four coils were connected in series in such a way that when current flowed in the circuit a pure pitching moment was imposed on the system. This applied also to each spindle separately, and either could be used independently for making tests with a finite aspect-ratio model.

When the system was oscillated, the phase of the alternating driving current was set to be in quadrature with the displacement in order to give a moment in phase with the damping moment. By adjusting the magnitude and sign of the current the damping moment could be balanced and a sustained oscillation obtained.

2.3. *Displacement Pickup.* The function of the displacement pickup was twofold, first to give a measure of the amplitude of oscillation, and second to provide a signal for the driving amplifier which supplied current to the exciter coils, and thus to complete the feedback loop which enabled self-excitation to take place. A photocell type of pickup, illustrated in Fig. 1, was devised for this purpose. By means of a lamp and lens a parallel beam of light was formed and then brought to a focus on a white screen by a second lens. The image on the screen acted as a light source illuminating

a vacuum-type photocell which was screened from the direct light from the lamp. A metal vane fixed to one of the driving coil arms partially intercepted the parallel beam, and a suitably shaped mask placed near the vane ensured a linear relation between image intensity and angular displacement of the system. The indirect illumination of the photocell obtained with this arrangement avoided non-linearities due to non-uniform sensitivity of the cathode surface.

In order to obtain a high pickup sensitivity a large load resistance (22 megohm) was employed in the photocell circuit, and to minimise the shunting effect of lead capacity on this load the cathode of the photocell was connected by a short length of wire to the grid of a cathode-follower. The small phase shift due to residual stray capacity was compensated at each working frequency by an adjustable RC coupling circuit connected to the cathode-follower output.

A rapid d.c. calibration of the pickup could be made by rotating a metal shutter into the path of the parallel beam of light. This removed a fraction of the light forming the image on the screen known to correspond to a certain angular displacement of the system. The sensitivity of the pickup could be varied by adjusting the lamp current, and it was normally set to give an output of 1 volt peak when the system was oscillating.

For the measurement of amplitude the signal from the pickup was first amplified by a highly stable negative-feedback amplifier (intrinsic gain 3000, gain with feedback 67) and then rectified with a full-wave instrument rectifier, the resulting direct current being measured with an accurate microammeter.

2.4. *Control Unit.* The maintenance of a stable amplitude of oscillation of a self-excited system requires some form of automatic control mechanism which adjusts the driving power to compensate for changes in damping on the system. Where the damping arises from air-flow in a wind tunnel some more or less rapid fluctuation must be expected, and the control requires to be rapid in action.

The method employed was completely electronic and is illustrated in Fig. 2. The signal from the displacement pickup was first amplified to a level of approximately 60 volts peak and then fed to a trigger circuit of the Schmitt type which produced a constant amplitude square wave of the same frequency and phase as the pickup signal. A differencing circuit followed in which a controllable fraction of the pickup signal was subtracted from the square wave, and finally an RC filter circuit removed harmonic components to leave a sinusoidal signal of amplitude equal to a constant less some fraction of the amplitude of the pickup output. By using this signal as the input to the driving amplifier a controlled system was obtained in which a change in amplitude of oscillation resulted in a change of opposite sign in the amplitude of the signal to the amplifier and thus altered the driving power in a direction tending to restore the amplitude of oscillation to its original value. The tightness of control could be varied by adjusting the fraction of the pickup signal subtracted from the square wave.

The method of control described above is much more rapid in action than the conventional A.G.C. technique in which the pickup signal is amplified, rectified and smoothed to provide a d.c. potential for biasing back a variable gain valve in the driving amplifier. This greater rapidity results from the nature of the filtering employed, which in the first case is required to remove harmonics and leave the fundamental, whereas in the conventional A.G.C. method it must remove the whole of the alternating components and thus involves much larger time constants. It has been found also that the lag in response with the latter method is prone to give relaxation oscillations of the combined electromechanical system.

2.5. *Driving Amplifier and Phase Shifter.* A conventional push-pull amplifier (Fig. 4) was employed, with a maximum output of 17 watts. The driver stage consisted of a long-tailed pair acting as a phase splitter, and a negative feedback signal was fed to the grid normally held at a fixed potential. Variable current feedback was employed and was derived from a low-resistance potentiometer in series with the output-transformer secondary winding.

The first stage of the amplifier, which preceded the phase splitter, was designed to act as a phase shifter and comprised a pair of valves coupled by a conventional see-saw arrangement to give equal and opposite output signals at the cathodes. A fixed capacity and a variable resistance were connected in series across the cathodes, and a high-resistance potentiometer connected their junction point to one of the cathodes. At each working frequency the variable resistance was adjusted to have the same impedance as the condenser, and with this condition the signal fed to the phase splitter from the potentiometer, could be shifted in phase by amounts varying from 0 deg to 90 deg relative to the input by rotating the wiper away from the valve cathode. The variation of signal amplitude over this range amounted to $\pm$ 20 per cent on a mean value. The direction of the phase shift could be reversed by interchanging the capacity and variable resistance by means of a switch (not shown in Fig. 4).

2.6. *Electronic Wattmeter.* The measurement of driving power required a wattmeter with ranges extending from a few milliwatts up to several watts, and since it was also desirable, from considerations of accuracy, to use the wattmeter as a null indicator in setting the driving current in quadrature with the displacement, a further requirement was a fairly high input impedance to avoid the introduction of phase shifts in the circuits supplying the relevant signals. Since at the time there appeared to be no commercial instrument available which satisfied these requirements, an electronic wattmeter was developed based on the work of Mallett[2].

Basically the action of the wattmeter depends on a pair of valves with identical square-law characteristics. If the sum $v_1 + v_2$ of two sinusoidal signals is applied to the grid of one of the valves and the difference $v_1 - v_2$ to the grid of the other, a difference between the mean currents in the valves is produced which is proportional to $v_1 v_2 \cos \epsilon$, where ϵ is the phase angle between v_1 and v_2. This difference may be conveniently observed as a steady voltage across the valve anodes by including equal resistances in the anode circuits.

The essential features of the circuitry developed are illustrated in Fig. 5. The input stage consisted of a double triode V_1 forming a long-tailed pair, with a pentode V_2 as the common cathode load. A signal applied to the grid of V_2 appeared at the anodes of V_1 with the same sign and equal amplitudes, whereas a signal fed into V_1 appeared with equal amplitudes but opposite sign. Thus the signals applied to the square-law valves V_3 and V_4 were of the form $av_1 + bv_2$ and $av_1 - bv_2$, and the steady potential developed between the anodes was proportional to $abv_1v_2 \cos \epsilon$. The voltage changes at the anodes were applied to the grids of a balanced pair of cathode-followers V_5 and V_6 via resistance networks incorporating two stages of RC filtering for removing the sinusoidal components, and the voltage change between the cathodes of V_5 and V_6 was measured directly with a sensitive d.c. instrument. Two stages of RC coupling between V_1 and the square-law valves were employed in order to minimise voltage surges due to switching operations.

A number of different valve types were tested in searching for square-law characteristics, and the EF 54 was selected as the type maintaining the required characteristic over the greatest range of control grid voltage. Since it is virtually impossible to find two valves giving exactly equal outputs, the valve with the greater output received its input from a potentiometer P_1. Likewise inequality

between the two halves of V_1 was balanced with the potentiometer P_2 which adjusted the relative amounts of negative feedback at the cathodes. The setting-up process for the instrument consisted in adjusting P_1 and P_2 to give a null reading on the meter with a signal supplied to each input in turn. A d.c. balance was obtained by adjusting the bias of V_4. In order to obtain an acceptable zero stability it was found essential to use a well stabilized **H.T.** supply and to run the heaters of $V_3 - V_6$ from an accumulator. Bias for V_3 and V_4 was also obtained from a battery.

Full-scale meter deflection was obtained with input signals of approximately 0·1 volt peak. These signals were supplied via precision 10,000 ohm 3-decade voltage dividers, one of which was connected across a resistance placed in series with the driving coils, with one side earthed, to give a voltage proportional to current, the other being connected through a 100,000 ohm resistance to the 'live' end of the driving coil chain for measuring power, or to the output of the displacement pickup for setting phase. The voltage dividers performed the function of 'range changing' switches, and enabled a very wide range of powers to be measured. For greatest accuracy the voltage dividers were normally set to supply equal input voltages to the wattmeter, which was attained by adjusting each divider in turn to give the same meter reading when switched to supply both inputs.

2.7. *Frequency Meter.* The determination of the aerodynamic stiffness derivatives from measurements of the change in natural frequency of the oscillating system due to the wind loading required an accurate method of measuring small frequency changes, since it was estimated that in the worst case these might not be more than 1 per cent. The method adopted was based on the Maxwell bridge and is illustrated in Fig. 3. In this arrangement a high-speed relay (Siemens type) operated by the square wave from the control circuit through a driving valve was made to charge a condenser C to a potential V and to discharge it through a resistance network including R and P once per cycle of oscillation. The average current flowing through the galvanometer G was thus proportional to frequency and could be balanced to give a null reading by adjusting the voltage divider P. Unsteady components of the current were removed by an RC filter.

The voltage divider P was a three-decade precision instrument, and by limiting settings to values not greater than 100 in order to minimise changes in the network impedance, a relation between frequency and setting was obtained which was linear to within $\frac{1}{2}$ per cent. The calibration of the bridge could be varied by means of the variable resistance S, and it was normally adjusted to give voltage-divider settings numerically equal to the frequency at balance. This adjustment could be rapidly checked by feeding in an accurate 100 cycle signal derived from the N.P.L. standard frequency source, and setting the voltage divider to read 100.

In measuring a frequency, voltage-divider settings differing by unity were found which gave galvanometer deflections on opposite sides of zero. From measurements of these deflections it was then possible to interpolate between the voltage-divider readings. The overall stability of the instrument was such that frequencies of 10 cycles per second could be read to 1 part in 10^4. This enabled frequency changes as small as 1 per cent to be measured to an accuracy of 1 per cent plus a maximum calibration error of $\frac{1}{2}$ per cent.

For some conditions still smaller changes in frequency were obtained, and these were measured by a beat method in which the signal from the displacement pickup was applied to the beam of an oscilloscope together with the N.P.L. standard 1,000 cycle signal. The time base of the oscilloscope was synchronised to a convenient sub-multiple of the standard frequency, and the beat frequency, observed as a periodic y-displacement of the 1,000 cycle trace at a fixed x-position, was measured with a stopwatch.

2.8. *Electrical Loss Measurement.* In deriving the damping for the oscillating system from the power measurement a correction was required for the power losses due to the ohmic resistance in the driving coil circuit, to eddy currents in neighbouring metallic parts of the structure and to hysteresis effects in the magnetic material of the exciter magnets. These losses were determined directly from a single power measurement with the oscillating system clamped and a current flowing in the driving coils equal in magnitude and frequency to the current with the system oscillating. The current was obtained by supplying the driving amplifier with an input signal from a variable-frequency valve oscillator, and the system was clamped by a brake mechanism in which spring-loaded friction blocks were brought into contact with the spindles from both sides.

The brake mechanism also served as a safety device where negative aerodynamic damping was encountered, and for this purpose it was tripped automatically when the amplitude of oscillation reached a predetermined value. Normally the brake blocks were held clear of the spindles by means of toggles held in by electromagnets. The current in the latter was momentarily interrupted and the toggles were released when a contact spring was deflected by an arm attached to one of the spindles.

2.9. *Calibration of Wattmeter and Amplitude Meter.* In order to determine the true power corresponding to a given electronic wattmeter reading use was made of a 20 ohm resistive load which could be switched into the driving amplifier in place of the driving coils. A signal of the required frequency was supplied to the amplifier from a valve oscillator, and the power in the load was measured by the electronic wattmeter and a substandard dynamometer wattmeter simultaneously. The power was adjusted to give a large deflection on the dynamometer instrument, and the voltage dividers were set to give the required reading on the electronic wattmeter. A relation was thus obtained between power and voltage-divider settings for this reading. When the power required to oscillate the mechanical system was large enough to be measured with sufficient accuracy directly on the dynamometer wattmeter, the electronic instrument was not used.

The calibration relating to amplitude measurement was divided into two parts, first a d.c. calibration of the displacement pickup, and then an a.c. calibration of the associated amplitude amplifier with rectifier and microammeter. The d.c. calibration was effected by measuring the output voltage from the pickup obtained on operating the metal calibrating shutter (*see* Section 2.3). A null method was used in which the output voltage was balanced against an equal voltage derived from an accumulator by means of a precision 4-decade voltage divider, the voltage across the accumulator being measured with a sub-standard dynamometer voltmeter. For the a.c. calibration the driving amplifier was employed with the resistive load and input from the valve oscillator. The voltage divider was connected across the load and used to supply a signal to the amplitude amplifier, the a.c. voltage across the load being measured with the same dynamometer voltmeter as was used for the d.c. calibration. These two calibrations determined the a.c. input to the amplitude amplifier corresponding to a given microammeter reading and the d.c. output from the displacement pickup for a given angular displacement and thus enabled a relation between microammeter reading and amplitude of oscillation to be obtained.

2.10. *Eddy-Current Damper.* Where negative aerodynamic damping was encountered greater in magnitude than the apparatus damping, the mechanical system was excited aerodynamically without the aid of the electrical drive. To deal with this case an eddy-current damper was brought into action consisting of two aluminium vanes one fixed to each spindle and arranged to oscillate in the field gaps of a pair of electromagnets (not shown in Fig. 1). By adjusting the current in the

magnet windings to make the total damping positive, measurements could be made in the usual way and the aerodynamic damping obtained as a difference between measurements with and without the wind.

2.11. *Test Procedure.* Before commencing a series of measurements the calibration of the frequency meter was adjusted and the amplitude meter was calibrated in the manner described in Section 2.9. Frequent checks of these calibrations were made during the tests. Measurements of driving power, current and frequency were made with the system oscillating at the required amplitude and the current set in quadrature with the motion, both with the tunnel running and in still air; electrical loss measurements and electronic wattmeter calibrations followed immediately.

The still-air driving power, corrected for loss, represented the apparatus damping, which was assumed to be due to elastic hysteresis in the torsion bars and at their clamping surfaces. On this basis the driving power in still air with a given torsion bar would be proportional to frequency, and the damping derivative $M_{\dot{\theta}}$ was calculated from the formula

$$W - \lambda W' = -26{\cdot}77 f^2 \theta_0^2 M_{\dot{\theta}}, \tag{1}$$

where λ is the ratio of frequency in the wind to that in still air and corrects the still-air power W' for the change in frequency due to wind loading. In this formula power is in watts and θ_0 in radians.

The stiffness derivative M_θ was calculated from the formula

$$M_\theta = \sigma_\theta (f+f_0)(f-f_0)/f_0^2 \tag{2}$$

involving the frequencies with and without the wind and the elastic stiffness σ_θ of the torsion bar assembly, which was obtained from a static test.

Effects of neglecting the still-air damping and inertia on the moving parts not exposed to the wind and on the model in the tunnel working section were examined by separate experiments and are discussed in Appendix I.

3. *Experimental Results.* 3.1. *Details of Models.* All the models tested were constructed of solid steel with flat rectangular end lugs for clamping to the oscillating spindles. The subsonic tests were made for one axis position only, which was positioned at the c.g. of the RAE 104 profile, coinciding with the mid-point of the lug section. In the case of the supersonic tests four axis positions were employed, namely, at the leading-edge, quarter-chord, half-chord and three-quarter chord positions. These were obtained with separate models in which the biconvex profile was suitably positioned in relation to the end lugs. Since the profile was symmetrical about the mid-chord position, a single model served for the quarter-chord and three-quarter chord tests. The object in employing separate models for the different axis positions in this case was to maintain a maximum clamping efficiency at the spindles with a minimum inertia; and since a rapid technique for making two-dimensional models with simple profiles had been evolved, based on a tangent plane approach, duplication of models was regarded as acceptable. The models tested are listed in Table 1 below.

TABLE 1

Model	1	2	3	4	5	6
Profile	RAE 104	RAE 104	Biconvex	Biconvex	Biconvex	Biconvex
Aspect ratio	∞	4	∞	∞	∞	∞
Thickness/chord (per cent)	10	10	7·5	7·5	7·5	5
Axis position (from L.E.)	0·445	0·445	0	0·25 0·75	0·5	0·5
Chord (in.)	2·0	2·5	2·0	2·0	2·0	2·0
Span (in.)	9·5	5	9·5	9·5	9·5	9·5

3.2. *General Remarks on Tests.* The procedure followed in making the subsonic tests was to run through the Mach number range for each still-air natural frequency, determined by the torsion bar stiffness, to obtain basic experimental curves of $m_{\dot{\theta}}$ and m_{θ} plotted against M. Since only small changes in frequency occurred with change in Mach number, the frequency parameter ω varied approximately inversely as the wind speed, and in general this variation has been plotted against M in the basic-curve diagrams. Curves showing the variation of the derivative coefficients with ω for constant M have been obtained by cross-plotting from the basic curves.

Measurements at mean incidences other than 0 deg were complicated at the lowest frequency by change in incidence with Mach number due to twist of the torsion bars under the mean aerodynamic moment. In these cases the model was set by trial and error to give the required mean incidence approximately at transonic speeds, and curves showing the variation of mean incidence with Mach number are included in the Figures. At the higher frequencies the torsion bars were sufficiently stiff to prevent any appreciable change in incidence.

The subsonic measurements were made with solid liners fitted to the tunnel, and required correction for blockage effects. Corrections appropriate to static tests were used, since the dynamic case has not yet been treated theoretically, and in the finite aspect-ratio tests the method of the equivalent doublet and its images as described by Thompson[3] was applied. In estimating the wake blockage, existing values of the drag coefficient were utilized. For the two-dimensional tests blockage corrections were calculated from tunnel wall pressures in the manner described by Mair and Gamble[4].

The basic curves for the supersonic tests, were formed by running through the amplitude range for each still-air frequency, Mach number and axis position. By cross-plotting, curves of damping and stiffness against ω for fixed θ_0, M and h, and against h for fixed ω, θ_0 and M were obtained.

The semi leading-edge angle for the $7\frac{1}{2}$ per cent thick biconvex profile is $8 \cdot 58$ deg. This is the deviation of the flow when the model is at 0 deg incidence, and for this condition the bow wave is attached at both the test Mach numbers. At the lower Mach number ($M = 1 \cdot 42$) the bow wave becomes detached for deviations greater than $9 \cdot 97$ deg, thus in the oscillatory tests it may be assumed that the bow wave was detached for part of the cycle for amplitudes greater than $1 \cdot 39$ deg. At the higher Mach number ($M = 1 \cdot 61$) the bow wave was attached for all conditions of the tests. Estimates of the position of shocks reflected from the tunnel walls indicate that for all conditions, both with attached and detached bow waves, these are well clear of the model.

3.3. *Two-dimensional subsonic Tests*.* The measurements were made on a model with a 10% RAE 104 profile oscillating about an axis at a distance $0 \cdot 445c$ behind the leading edge (model 1, Section 3.1). This particular axis coincided with the c.g. of the section and thus avoided the possibility of errors due to coupled inertial forces arising from flexure of the model. The test still-air frequencies ranged from $11 \cdot 5$ c.p.s. to 68 c.p.s. approximately and the Mach number from $0 \cdot 3$ to $0 \cdot 9$. Tests were made at mean incidences of 0, 2 and 3 deg and amplitudes of oscillation of 1 and 2 deg. At the higher Mach numbers the frequency parameter ranged from $0 \cdot 01$ to $0 \cdot 08$, and a Reynolds number of $0 \cdot 8 \times 10^6$ was attained.

* The subsonic results given in this report supersede earlier measurements, some of which appear in Ref. 15. The earlier tests were subject to considerable unsteadiness in the tunnel flow and are thought to be unreliable on this account. Improved flow conditions were obtained by modification to the tunnel intake before the present tests were commenced.

3.3.1. *Tests at* 0 *deg mean incidence.* Experimental curves showing the variation of $-m_{\dot{\theta}}$ and $-m_{\theta}$ with Mach number at three still-air frequencies are shown in Figs. 7 and 8 for a mean incidence of 0 deg. At low Mach numbers the damping curves are flat, but a rapid increase in damping takes place as M is raised, a peak value being reached at approximately $M = 0{\cdot}81$, which is somewhat higher than the critical Mach number (pressure critical)[5]. For further increase in Mach number the damping falls rapidly. The effect of amplitude of oscillation is small, being greatest near the peak value of the damping, which is greater for the small amplitude. The general shape of the curves is unaffected by frequency over the range covered, particularly in relation to the position of the peak damping.

The numerical value of the stiffness $-m_{\theta}$ shows a similar but much smaller increase up to $M = 0{\cdot}8$ approximately. This is followed by a minimum and second maximum at $M = 0{\cdot}89$. As in the case of the damping, frequency has little effect on the shape of the curves, and amplitude effects are small.

Tests were also made with a turbulent boundary layer on the model in the case of the middle frequency. For this purpose a coating of carborundum powder was applied to the model with an adhesive, extending from the leading edge for a distance of $0{\cdot}1c$. The grade of carborundum powder and the density of distribution of the grains were selected to give a drag, as measured by a wake traverse at zero incidence, equal to the known drag for this profile with a turbulent boundary layer. The wake traverse tests were made at $M = 0{\cdot}5$ and $0{\cdot}75$.

Curves of damping and stiffness for the turbulent boundary-layer condition are included in Figs. 7 and 8. The only significant difference when compared with the curves for natural transition is the disappearance of the second maximum in the stiffness curve. However, since this occurs at the end of the Mach number range, it is probable that it now appears at a slightly higher value of M.

3.3.2. *Tests at mean incidences of* 2 *deg and* 3 *deg.* The major effect of incidence on $-m_{\dot{\theta}}$ and $-m_{\theta}$ occurs at the higher Mach numbers in the region between $M = 0{\cdot}75$ and $0{\cdot}9$. At a mean incidence of 2 deg (Figs. 9 and 10) and the lowest frequency the fall-off in damping is more rapid, and leads to a narrow region of negative damping in the neighbourhood of $M = 0{\cdot}87$. With further increase of Mach number a rapid rise to positive values takes place. At the higher frequencies the peak damping is reduced and occurs at a lower Mach number ($M = 0{\cdot}77$ approx.). This is followed by a minimum and a second smaller peak leading into a rapid fall-off, but the damping remains positive.

At a mean incidence of 3 deg (Figs. 11 to 13) and at the lowest frequency the region of negative damping has become very deep and large amplitude effects are present, the damping being more negative for the smaller amplitude. At the higher frequencies the curves are similar to the 2 deg mean incidence case in general shape, the minimum, however, is more pronounced and the final fall-off leads to negative damping.

The stiffness curves for a mean incidence of 2 deg and 3 deg are affected very little by frequency, and they differ from the 0 deg case in that the second numerical maximum has become smaller and at 3 deg has almost vanished. The first maximum occurs at a progressively lower Mach number as the mean incidence is raised.

Curves of damping and stiffness for the turbulent boundary-layer condition are included in Figs. 12 and 13, and a comparison with corresponding curves for natural transition shows no significant difference.

It is difficult to offer a physical explanation for the sudden changes and loss in damping at the higher Mach numbers observed in the tests discussed above without a detailed knowledge of the pressure distributions and flow conditions. It seems likely, however, that the effects are associated with flow separation due to the presence of shock waves on the surfaces of the model.

3.3.3. *Comparison with theory.* In comparing the experimental results with theory it is important to consider the effect of tunnel wall interference, since it has been shown theoretically by W. P. Jones[6] that this would be large for two-dimensional flow in the case of the damping derivative at the small values of frequency parameter attained and for the size of tunnel and axis of oscillation employed. This is illustrated by the curves in Fig. 14, which are taken from a report by Jones[6] and show the effect of the tunnel wall interference on flat-plate theory for $M = 0$ and $0{\cdot}7$. Curves based on the equivalent profile theory[6], together with the influence of tunnel interference, appropriate to the conditions of the present tests, are also included. This introduces the effect of aerofoil thickness and boundary layer into the theory.

In view of the large tunnel interference effects predicted by theory, no attempt has been made to correct the experimental results to free-stream conditions, and the comparisons with W. P. Jones given in Figs. 7 and 8 are with equivalent profile theory including the effects of the tunnel walls. Agreement is satisfactory up to the peak value of the damping (Fig. 7), but the theory predicts a fall-off at a considerably higher Mach number. Free-stream flat-plate theoretical damping curves are also included in Fig. 7, and it will be noticed that these approach the experimental curves more closely the higher the frequency. This agrees with the prediction (Fig. 14) that the tunnel wall effects will become smaller as the frequency parameter is raised. The theoretical result by W. P. Jones and flat-plate theory both show good agreement with the stiffness curves (Fig. 8).

3.4. *Subsonic Tests with Spoilers.* For the purpose of these tests spoilers were fixed to the two-dimensional RAE 104 model, and measurements were made at subsonic speeds at a nominal still-air frequency of 36 c.p.s., with an amplitude of oscillation of 2 deg and mean incidences of 0 deg and 3 deg. Three different spoilers were used, two being uniform in the spanwise direction and square in section with sides of $0{\cdot}02$ in. and $0{\cdot}04$ in. respectively. The third was a castellated spoiler formed by cutting $0{\cdot}035$ in. square teeth on a uniform $0{\cdot}045$ in. square-section spoiler, the pitch of the teeth being equal to twice their width. The spoilers were made of steel and were attached with Araldite.

Most of the tests were made with the spoilers fixed at the trailing edge of the model, either on one surface or on both surfaces together. Some of the tests with the $0{\cdot}04$ in. spoiler, however, were made with the spoiler at the $0{\cdot}65$ chord position. For all these tests the model boundary layer was made turbulent.

3.4.1. *Spoiler tests at 0 deg mean incidence.* The effects of the $0{\cdot}02$ in. and $0{\cdot}04$ in. square-section spoilers on the damping derivative $-m_{\dot{\theta}}$ when placed at the trailing edge are compared in Figs. 15a and 15b. A single small spoiler has little effect on the damping curve, but two spoilers, one on each surface, produce a rapid loss of damping above $M = 0{\cdot}8$, with a region of negative damping between $M = 0{\cdot}84$ and $0{\cdot}90$ approximately. In the case of the larger size, a single spoiler now leads to a considerable loss of damping above $M = 0{\cdot}76$, zero damping being reached at $M = 0{\cdot}87$. Two spoilers produce an extremely violent fall-off in damping above $M = 0{\cdot}8$ with no sign of recovery up to the highest Mach number of the tests.

Positioning the 0·04 in. spoiler at 0·65c from the leading edge has a markedly different effect from that of the trailing-edge position. A single spoiler produces a loss of damping between $M = 0{\cdot}76$ and 0·88 with full recovery at the latter Mach number (Fig. 16a), whereas two spoilers give a curve similar in shape to the case with no spoilers, but with smaller damping on the whole. In both cases the damping at the lower Mach numbers ($M = 0{\cdot}4$) is much reduced.

During the tests with the square-section spoilers a suggestion was made that the rapid loss of damping at the higher Mach numbers might be associated with the formation of two-dimensional vortices by the spoilers, and that a castellated spoiler might reduce this loss of damping by breaking up the regular vortices to give a more random flow pattern. Damping curves for a castellated spoiler, given in Fig. 17a, have a similar shape to the curves for the smaller square-section spoiler (Fig. 15c), but show a somewhat greater fall-off in the higher Mach number region. In fact, in this region the curves are intermediate between those for the two square-section spoilers, and since the mean height of the castellated spoiler is also intermediate (0·028 in. as compared with 0·02 in. and 0·04 in.) it appears that this may be the effective parameter rather than the castellated profile.

The effect of the spoilers on aerodynamic stiffness is shown in Figs. 19 to 22, in which the negative stiffness (m_θ instead of $-m_\theta$) is plotted, since this brings out a marked similarity with the effect on damping. The curves relating to the uniform spoilers at the trailing edge (Fig. 9) show a falling off and change in sign of m_θ almost identical with that for $-m_{\dot\theta}$ (Fig. 15), the exception being the case of the smaller spoiler on one surface, which appears to have more effect on m_θ than on the damping. Similar correlation exists for the castellated spoiler (Fig. 21), the region of negative m_θ, however, being somewhat narrower than for $-m_{\dot\theta}$. In the case of the spoilers at the 0·65c position (Fig. 20), the similarity with the damping curves is not so close. The initial drop with one spoiler occurs at approximately the same Mach number as for the damping (Fig. 16a), but is quickly followed by a rise and second maximum. With two spoilers the curve is closer in shape to that without spoilers, as in the case of the damping.

3.4.2. *Spoiler tests at* 3 *deg mean incidence.* In general the effect of the spoilers is to accentuate any falling-off in damping or m_θ in the high Mach number region. Damping curves for the uniform spoilers at the trailing-edge position (Figs. 16b and 18) show this as a lowering of the minimum in the curve obtained without spoilers, with the formation of regions of negative damping. It is clear from Fig. 18b that, on the whole, a spoiler on the upper (suction) surface has less effect than one on the lower surface. This also applies to m_θ as shown by Fig. 22b.

The effect of 0·04 in. square spoilers at the 0·65c position is very similar to that for 0 deg mean incidence. With two spoilers the trend is for the shape of the original curve to be maintained, both in the case of damping (Fig. 16b) and m_θ (Fig. 20b); with a single spoiler on the lower surface, however, an earlier falling-off in both damping and m_θ is obtained.

In the case of the castellated spoilers the fall in the original damping and m_θ curves is now continued to negative values, and there is not a great deal of difference between the effect of a single spoiler on the lower surface and two spoilers, one on each surface (Figs. 17b and 21b).

3.5. *Finite Aspect Ratio Subsonic Tests.* These tests were made on a rectangular model of aspect ratio 4 (tip-to-tip aspect ratio) using the half model technique (model 2, Section 3.1). The profile and axis were the same as for the two-dimensional subsonic model, and the still-air frequencies ranged from 11 c.p.s. to 57 c.p.s. approximately. Measurements were made at mean incidences of

0 deg and 3 deg, and amplitudes of oscillation of 1 deg and 2 deg, for Mach numbers ranging from 0·3 to 0·93. At the higher Mach numbers the frequency parameter varied from 0·01 to 0·1 approximately and a Reynolds number of $1{\cdot}0 \times 10^6$ was obtained.

3.5.1. *Experimental results.* Curves showing the variation of $-m_{\dot{\theta}}$ and $-m_{\theta}$ with Mach number are given in Figs. 23 to 26, and these are cross-plotted in Fig. 27 to show the effect of frequency parameter. The damping curves for 0 deg mean incidence (Fig. 23) show a rise with Mach number to a peak value on approaching $M = 0{\cdot}9$, which occurs somewhat earlier at the lowest frequency. At a mean incidence of 3 deg (Fig. 25) the peak is still further delayed and occurs approximately at $M = 0{\cdot}92$. A small amplitude effect is also apparent on the rising part of the 3 deg mean-incidence curves, the damping being greater for the larger amplitude of oscillation.

The stiffness curves for both 0 deg and 3 deg mean incidence fall slightly with increasing Mach number to give a minimum a little above $M = 0{\cdot}8$ followed immediately by a maximum at $M = 0{\cdot}9$. The minimum is more pronounced in the curves for 3 deg incidence, whilst in the curves for zero incidence a small amplitude effect appears above the minimum, the stiffness being numerically smaller for the larger amplitude.

Apart from the difference in magnitude, the major difference between the results for $A = 4$ and $A = \infty$ (*see* Figs. 7 and 8, and 11 to 13) is that in the case of the finite aspect ratio any fall-off in damping is considerably delayed and fluctuations in the stiffness at the higher Mach numbers are reduced.

The variation of both damping and stiffness with frequency parameter (Fig. 27) is not large over the range covered, and amounts to a reduction in magnitude with increasing ω up to $\omega = 0{\cdot}1$ approximately, after which the curves tend to flatten out. A comparison between results for mean incidence of 0 deg and 3 deg is also given in Fig. 27.

3.5.2. *Comparison with theory.* Available theoretical points for the aspect ratio and axis position of the tests are included in Figs. 23 and 24. With the exception of the single point at $M = 0{\cdot}846$ these values correspond to the frequency parameter shown in the experimental curves; the points at $M = 0{\cdot}3$, however, are strictly theoretical values for $M = 0$. The point at $M = 0{\cdot}846$ relates to $\omega \to 0$.

The three points due to Lehrian[7] derive from an 'equivalent' wing theory[8] using a vortex lattice method of downwash calculation, the values at $M = 0{\cdot}866$ being corrected to an exact value of the downwash at the centre of the wing, in accordance with calculations by Acum[9]. These points define damping curves which are somewhat flatter than the experimental curves, but the agreement is reasonably good at the lower Mach number and near the peak value of the damping, especially in the case of the tests at the lowest frequency.

The single points at $M = 0{\cdot}866$ due to Acum are derived from an extension to general Mach number and frequency parameter of the low frequency Multhopp-Garner theory[10]. For the low values of the frequency parameter under consideration these results differ little from the corresponding values due to Lehrian. The points due to Acum and the low frequency Multhopp-Garner values at $M = 0{\cdot}846$ are both in fair agreement with the damping measurements.

All the theoretical values show satisfactory agreement with the stiffness curves.

Wind-tunnel interference effects have not been indicated here since numerical values are not available.

3.6. *Two-Dimensional Supersonic Tests.* Most of these measurements were made with a $7\frac{1}{2}$ per cent biconvex aerofoil oscillating about axes at the leading edge, and at positions $0{\cdot}25c$, $0{\cdot}50c$ and $0{\cdot}75c$ behind the leading edge in turn. The tests were made at Mach numbers of $1{\cdot}42$ and $1{\cdot}61$ with torsion bars giving still-air frequencies ranging from $11{\cdot}5$ c.p.s. to 58 c.p.s. approximately, and the amplitude of oscillation was varied from 1 deg to 4 deg in steps of 1 deg. The frequency parameter ranged from $0{\cdot}006$ to $0{\cdot}046$ at $M = 1{\cdot}42$ and $0{\cdot}008$ to $0{\cdot}043$ at $M = 1{\cdot}61$, and a Reynolds number of approximately $0{\cdot}8 \times 10^6$ was obtained. All the measurements were made at a mean incidence of 0 deg.

A small number of tests were made with a 5 per cent biconvex model oscillating about the mid-chord axis.

3.6.1. *Tests at $M = 1{\cdot}42$.* The variation of $-m_{\dot\theta}$ and m_θ with amplitude of oscillation is shown in Figs. 28 to 31 for the range of axis positions and frequency parameter values covered in the tests. For the most forward axis position (Fig. 28c) the derivative $-m_{\dot\theta}$ decreases (increase in negative value) with increase in amplitude θ_0, the decrease becoming smaller at the lower values of the frequency parameter. This decrease with increasing θ_0 tends to become smaller as the axis is moved aft, and at the mid-chord position it has changed sign at the lowest frequency parameter to become a small increase. Results for the $0{\cdot}75c$ axis position show an increase with θ_0 for all values of ω.

In the case of m_θ a similar but smaller decrease with increasing θ_0 is observed for the forward axis positions. Frequency parameter, however, appears to have little effect. Results for the rearmost axis position show practically no amplitude effect at all.

Curves of $-m_{\dot\theta}$ and m_θ relating to the 5 per cent biconvex model plotted in Figs. 30a and 30b all fall below the corresponding curves for the thicker section.

The effect of frequency parameter is shown in Fig. 32, which was obtained by cross-plotting from Figs. 28 to 31 at $\theta_0 = 2$ deg. Over the range covered it is clear that effects of ω are not large for this amplitude of oscillation.

The curves in Fig. 32 are further cross-plotted at $\omega = 0{\cdot}025$ to give Fig. 33, which shows the variation of $-m_{\dot\theta}$ and $-m_\theta$ with axis position at a fixed value of θ_0 and ω. Comparison is made in this Figure with earlier tests[1] made by the method of decaying oscillations for the mid-chord axis. Good agreement is obtained with $-m_\theta$, but $-m_{\dot\theta}$ shows considerable discrepancy, the damping for the earlier tests being considerably higher (*see* Section 3.6.2).

3.6.2. *Tests at $M = 1{\cdot}61$.* Amplitude effects for this Mach number are shown in Figs. 34 to 37. Broadly speaking, the effect on $-m_{\dot\theta}$ of increasing θ_0 is similar to that observed in the case of $M = 1{\cdot}42$; rearward movement of the axis, however, now produces a much smaller change in slope, and at the $0{\cdot}75c$ position $-m_{\dot\theta}$ still decreases with increase in θ_0. The results for $\omega \doteqdot 0{\cdot}034$ are inconsistent with the remaining curves, and in the case of the forward axis show practically no effect of amplitude. For the $0{\cdot}50c$ axis a rising curve is indicated, whilst for the rearmost axis the curve has become very non-linear with a marked dip in the neighbourhood of $\theta_0 = 1{\cdot}5$ deg. No explanation can be offered for this anomalous behaviour.

The variation of m_θ with θ_0 is much the same as for $M = 1{\cdot}42$, the curves becoming almost flat for the rearmost axis position.

As for the lower Mach number, curves of $-m_{\dot\theta}$ and m_θ for the 5 per cent biconvex model, plotted in Figs. 36a and 36b, fall below the curves for the thicker section.

Results for a turbulent boundary layer, obtained at $\theta_0 = 1{\cdot}5$ deg and 3 deg with $\omega \doteqdot 0{\cdot}025$, fall below the laminar-boundary curves at the L.E. and $0{\cdot}5c$ axis positions but show little change for the $0{\cdot}75c$ position. The turbulent boundary layer was created in this instance by forming on the upper and lower surfaces of the model a band of Frigilene 0·05 in. wide and 0·003 in. thick at $0{\cdot}05c$ from the leading edge.

For this Mach number the effect of frequency parameter on $-m_{\dot{\theta}}$, as shown by the cross-plot in Fig. 38, is somewhat more marked than for $M = 1{\cdot}42$, the value for the rearward axes increasing with increase in ω for the $7\frac{1}{2}$ per cent profile. For the 5 per cent profile the damping decreases with increasing ω. The stiffness $-m_{\theta}$ shows little change with ω, as before.

Fig. 39 presents the cross-plot at $\omega = 0{\cdot}025$ showing the variation of $-m_{\dot{\theta}}$ and $-m_{\theta}$ with axis position, corresponding to Fig. 32 for the $M = 1{\cdot}42$ case. Comparison is again made with the earlier decaying oscillation tests (*see* Section 3.6.1), and a similar discrepancy to that for the lower Mach number is evident. It is difficult to assign a reason for the large difference in damping. The decaying oscillation tests were made in a circular tunnel, and interference effects due to reflected shocks might be expected towards the ends of the model. These effects, however, appear to have been too small to make any appreciable difference in $-m_{\theta}$. A more likely explanation is effects due to model flexure. It can be seen from Figs. 48 to 51, relating to flexure in the present tests, that the effect has the correct sign for explaining the discrepancy in the damping, and that the effect on stiffness would be very small. It seems most likely that the earlier rig was considerably weaker in flexure than the present apparatus, since not only was the span greater (12 in.), but the end bearings were single and the built-in effect of the present double bearings was lacking. On the other hand, some attempt was made to increase flexural stiffness in the earlier apparatus by applying axial tension.

3.6.3. *Comparison with theory.* The experimental results given in Figs. 33 and 39 are compared in the same Figures with theoretical values based on flat-plate theory[11] and a theory due to Van Dyke[12] which introduces the effect of profile thickness. Good agreement with Van Dyke is obtained for rearward axis positions at both Mach numbers in the case of the damping $-m_{\dot{\theta}}$, but on approaching the leading-edge axis the experimental curves turn up less rapidly than the theoretical. Agreement between experimental and flat-plate curves is poor over the whole range of axis position, a point of particular interest being the mid-chord position near which flat-plate theory predicts a change in sign of the damping for $M = 1{\cdot}42$. The measured damping changes sign at an axis position considerably further forward ($h = 0{\cdot}344$), whilst Van Dyke predicts $h = 0{\cdot}442$ for this point. The experiments disagree completely with a theory due to Wylly[13], which predicts positive damping ($-m_{\dot{\theta}}$) for all axis positions and Mach numbers if the thickness is greater than 4·5 per cent*.

Measured values of the damping for the 5 per cent thick section ($h = 0{\cdot}5$) are smaller than for the $7\frac{1}{2}$ per cent model, which is in agreement with Van Dyke, the difference being considerably greater than given by theory, however.

The curves of stiffness derivative ($-m_{\theta}$) against axis position are nearly linear and have the same slope as the theoretical curves for the forward axis positions. Towards the rearward axis the slope becomes slightly less numerically, and the curves approach the theoretical values of Van Dyke. Agreement is closest with Van Dyke's theory, but the aerodynamic centre ($-m_{\theta} = 0$) lies further forward than predicted.

* Since shown to be incorrect (*see* A.R.C. 15,864).

As in the case of the damping, measured values of the stiffness for the 5 per cent thick section ($h = 0{\cdot}5$) are numerically smaller than for the thicker section, which again agrees with Van Dyke.

It has been suggested that departure from theory at the forward axis positions may be due to separation of flow towards the trailing edge. This would reduce the contribution of the pressures in this region, and its effect on the derivatives would be most marked for the forward axes. A comparison is made in Fig. 40 with curves based on a theory due to W. P. Jones[14]. This is a numerical theory and, since results are available only for $M = 1{\cdot}5$, comparison has been made with the mean of the experimental curves which corresponds to approximately the same Mach number. In one of the theoretical curves the integration of the pressures has been terminated at 70 per cent of the chord from the leading edge to simulate the effect of separation. In the case of the damping this gives much better agreement for the forward axes but is not quite so satisfactory at $h = 0{\cdot}75$. The effect on the stiffness is to displace the theoretical curve to the opposite side of the experimental curve, which suggests that still better agreement on the whole might have been obtained by extending the integration somewhat further towards the trailing edge.

To test the influence of pressures near the trailing edge a few measurements were made at $M = 1{\cdot}42$ with the axis at the leading edge, in which the chord was progressively reduced by cutting off squarely near the trailing edge. The results are given in Figs. 41 and 42. Unfortunately there is a considerable amount of scatter in the damping results, but it is fairly clear that for small amplitudes and the lowest frequency parameter removal of up to 20 per cent of the chord has little effect. The stiffness is unaffected by removal of up to 10 per cent of the chord. These results support the view that separation is making the rear part of the profile relatively ineffective.

The theoretical relationship between pitching damping and axis position h is parabolic in h and takes the form

$$m_{\dot{\theta}} = m_{\dot{\theta}}' + h(l_{\dot{\theta}}' - m_{\dot{z}}') - h^2 l_{\dot{z}}' \tag{3}$$

where the dashed symbols relate to the leading-edge axis, and $m_{\dot{\theta}}$ is the damping coefficient for an axis at h. Since measurements were made at four axis positions, including the leading edge, it is possible to derive from (3) three independent linear relationships between the unknowns $l_{\dot{\theta}}' - m_{\dot{z}}'$ and $l_{\dot{z}}'$. These are plotted in Fig. 43 for each Mach number, and from the error triangles formed by the intersection of the curves values for $l_{\dot{\theta}}' - m_{\dot{z}}'$ and $l_{\dot{\theta}}'$ which agree best with the experimental observations have been determined. By making use of the relations

$$l_{\dot{\theta}} - m_{\dot{z}} = l_{\dot{\theta}}' - m_{\dot{z}}' - 2hl_{\dot{z}}' \tag{4}$$

$$l_{\dot{z}} = l_{\dot{z}}' \tag{5}$$

the variation of $l_{\dot{\theta}} - m_{\dot{z}}$ and $l_{\dot{z}}$ with h has been determined and is compared with theory (Van Dyke) in Fig. 44. The slopes of the experimental curves for $l_{\dot{\theta}} - m_{\dot{z}}$ are considerably less than indicated by theory, large differences in actual value occuring at the forward and rearward axis positions. In the case of $M = 1{\cdot}42$ the experimental and theoretical values of $l_{\dot{\theta}} - m_{\dot{z}}$ for the leading-edge axis are of opposite sign. It is noteworthy, however, that almost exact agreement with theory is obtained for both Mach numbers at the mid-chord position. The experimental values of $l_{\dot{z}}$ are numerically considerably less than the theoretical values, agreement being closest for $M = 1{\cdot}61$.

A similar relation to (3) exists for the stiffness derivatives, but since the corresponding curves (Figs. 33 and 39) are nearly linear, it may be assumed that l_z' is zero, and values for $l_{\theta}' - m_z'$ can then be obtained from the mean slopes of the stiffness curves. The variation of $l_0 - m_z$ with h is

given by the corresponding relation to (4), which is independent of h when $l_z' = 0$. Values of $l_\theta - m_z$ are included in Fig. 44 and compared with theory, the agreement being satisfactory for both Mach numbers.

It should be pointed out that the theoretical estimates of the supersonic derivatives assume an attached bow wave, whereas in the tests at the lower Mach number the bow wave was detached for part of the cycle of oscillation at amplitudes above 1·39 deg. Since, however, the amplitude effect for $M = 1{\cdot}42$ is very similar to that for $M = 1{\cdot}61$ where the bow wave was always attached, it is argued that the effect of the bow wave becoming detached is small, and values of the derivatives for an amplitude of 2 deg were selected for comparison with theory, since these were regarded as being somewhat more accurate than the smaller amplitude results.

4. *Conclusions.* (1) The experience gained with the self-excitation technique showed that this was satisfactory at high speeds, and the equipment enabled measurements to be made at higher values of the frequency parameter than had been attained with earlier decaying-oscillation apparatus.

(2) The two-dimensional subsonic tests on the RAE 104 model at 0 deg mean incidence show a peak value of the damping at about $M = 0{\cdot}81$, which is somewhat higher than the critical Mach number, followed by a rapid fall-off. At mean incidences of 2 deg and 3 deg more complex changes occur, and at the lowest frequency a narrow range of Mach number exists around $M = 0{\cdot}87$ in which the damping is negative. At the higher frequencies this region of negative damping is suppressed, but in the case of the highest mean incidence the damping falls off to negative values as the upper limit of the Mach number range is approached.

The stiffness derivative shows corresponding, but less violent, changes with Mach number, and the effect of frequency is small.

Comparison of the damping measurements with two-dimensional flat-plate theory for free-stream conditions illustrates the large effect of the tunnel walls predicted by theory for low values of the frequency parameter, and shows how agreement is improved as the frequency is raised. Satisfactory agreement is obtained up to the peak value of the damping when comparison is made with a theory which includes tunnel wall effects and also the effects of aerofoil thickness and boundary layer introduced by an equivalent profile treatment. The fall-off in damping predicted by the theory is delayed, however. The measured stiffness derivatives show good agreement with free-stream flat-plate theory up to $M = 0{\cdot}8$.

(3) In general, spoilers fixed at the trailing edge of the model in the two-dimensional subsonic tests produce loss of damping at the higher Mach numbers, this loss being greater with a larger spoiler, or with two spoilers, one on each surface. Spoilers placed at the $0{\cdot}65c$ position have a different effect, a single spoiler producing a loss of damping over a range of Mach number with a subsequent recovery, whilst a spoiler on each surface tends to maintain the original shape of the damping curve. A roughly similar effect to that produced by the spoilers in the case of the damping curves is apparent also in the m_θ curves.

(4) Measurements on a rectangular wing of aspect ratio 4 at subsonic speeds with the same profile and axis as in the two-dimensional subsonic tests give curves similar to those obtained in the latter tests at 0 deg incidence, but with smaller numerical values for the derivatives. The peak in the damping curves appears at a somewhat higher Mach number, however, and the fluctuations in stiffness at the higher Mach numbers are reduced.

The effect of frequency parameter over the range covered is small.

Comparison with theory shows satisfactory agreement with the stiffness curves and reasonable agreement with the damping for the range of Mach number covered by theory.

(5) Two-dimensional supersonic tests on a $7\frac{1}{2}$ per cent biconvex model show definite amplitude effects over the range covered (1 deg to 4 deg). These effects depend on axis position, and to some extent on frequency parameter, and may be summarised roughly by stating that both $-m_{\dot{\theta}}$ and m_{θ} decrease with increasing amplitude for the L.E. axis position, this decrease becoming less as the axis is moved aft. The effect is greater for $-m_{\dot{\theta}}$ and for the smaller Mach number of the tests, in which case an actual increase in $-m_{\dot{\theta}}$ with increasing amplitude is obtained for the rearmost axis. Broadly speaking the effect of raising the frequency parameter is to increase the tendency of $-m_{\dot{\theta}}$ to fall with increasing amplitude. In the case of m_{θ} the effect is negligible.

For a fixed amplitude (2 deg) the effect of frequency parameter on $-m_{\dot{\theta}}$ and $-m_{\theta}$ is not large.

Comparison with theoretical curves showing the variation of $-m_{\dot{\theta}}$ with axis position shows closest agreement when the theory includes thickness effects (Van Dyke or W. P. Jones). Agreement is most satisfactory for rearward axes, considerable discrepancy existing for the forward positions. This is thought to be due in part to flow separations towards the T.E. reducing the contribution of pressures in this region, somewhat better agreement being obtained if the theoretical estimate ignores the integral of the pressures over the rear 30 per cent of the chord.

The curves of $-m_{\theta}$ against axis position are almost parallel to the theoretical curves and also agree more closely when the theory contains thickness effects. The bodily displacement of the experimental curve, however, indicates an aerodynamic centre somewhat ahead of the position predicted by theory. When the rear 30 per cent of the chord is ignored in the theory, the effect is not so satisfactory as in the case of $-m_{\dot{\theta}}$, the theoretical curve being displaced to the opposite side of the experimental curve.

Values of $-m_{\dot{\theta}}$ and m_{θ} obtained from tests with a 5 per cent biconvex model for the mid-chord axis position fall below the corresponding values for the $7\frac{1}{2}$ per cent biconvex model, a result which is in agreement with theoretical predictions.

The measurement of the direct pitching derivatives for several axis positions in the case of the $7\frac{1}{2}$ per cent biconvex model enabled values for $l_{\dot{\theta}} - m_{\dot{z}}$, $-l_{\dot{z}}$ and $l_{\theta} - m_{z}$ to be deduced. In comparison with theory (Van Dyke), $l_{\theta} - m_{z}$ shows good agreement, whereas the measured value of $-l_{\dot{z}}$ is high. Curves of $l_{\dot{\theta}} - m_{\dot{z}}$ against axis position have considerably smaller slopes than indicated by theory, but agreement is exact at the mid-chord position.

LIST OF SYMBOLS

a, b	Gains associated with long-tailed pair
c	Chord of wing
f	Pitching frequency
h	Distance of axis downstream of L.E. as fraction of c
l	Span of wing
l_z, $l_{\dot{z}}$	Coefficients in non-dimensional lift due to downward displacement $= l_z + j\omega l_{\dot{z}}$
l_θ, $l_{\dot{\theta}}$	Coefficients in non-dimensional lift due to pitching displacement $= l_\theta + j\omega l_{\dot{\theta}}$
m_z, $m_{\dot{z}}$	Coefficients in non-dimensional pitching moment due to downward displacement $= m_z + j\omega m_{\dot{z}}$
m_θ, $m_{\dot{\theta}}$	Coefficients in non-dimensional pitching moment due to pitching displacement $= m_\theta + j\omega m_{\dot{\theta}}$
δm_θ, $\delta m_{\dot{\theta}}$	Errors in m_θ and $m_{\dot{\theta}}$ due to flexure
p	Circular pitching frequency
p_z	Circular flexural frequency
v_1, v_2	Input voltages to long-tailed pair
z	Downward displacement of reference section
I_z	Inertia related to z-displacement
I_θ	Pitching inertia
δI_θ	Error in I_θ due to flexure
$L_z + jpL_{\dot{z}}$	$= \rho V^2 l \kappa_2 (l_z + j\omega l_{\dot{z}})$
$L_\theta + jpL_{\dot{\theta}}$	$= \rho V^2 c l \kappa_2 (l_\theta + j\omega l_{\dot{\theta}})$
$M_z + jpM_{\dot{z}}$	$= \rho V^2 c l \kappa_1 (m_z + j\omega m_{\dot{z}})$
$M_\theta + jpM_{\dot{\theta}}$	$= \rho V^2 c^2 l (m_\theta + j\omega m_{\dot{\theta}})$
$\delta M_\theta + jp\delta M_{\dot{\theta}}$	$= \rho V^2 c^2 l (\delta m_\theta + j\omega \delta m_{\dot{\theta}})$
M	Mach number
M_1	Driving moment
P	Product of inertia
$\bar{P}$	$= P/\rho c^3 l$

LIST OF SYMBOLS—*continued*

P'		Still-air damping power for model
V		Wind speed
W		Driving power in wind
W'		Driving power in still air
α		Mean incidence
ϵ		Phase angle between v_1 and v_2
η		Spanwise distance as fraction of span
θ_0		Amplitude of pitching motion
κ_1	$=$	$\int_0^1 f(\eta)d\eta$
κ_2	$=$	$\int_0^1 f^2(\eta)d\eta$
ν		Kinematic viscosity
ρ		Air density
σ_z		Flexural stiffness
$\bar{\sigma}_z$	$=$	$\sigma_z/\rho V^2 l$
σ_θ		Pitching stiffness
ω	$=$	pc/V frequency parameter

Dashed non-dimensional derivative coefficients relate to the leading-edge axis.

The suffix 0 denotes still-air frequency or a value of ω based on still-air frequency.

REFERENCES

No.	*Author*	*Title, etc.*
1	J. B. Bratt and A. Chinneck	Measurements of mid-chord pitching moment derivatives at high speeds. A.R.C. R. & M. 2680. June, 1947.
2	E. Mallet	A valve wattmeter. *J.I.E.E.* Vol. 73. p. 295. 1933.
3	J. S. Thompson	Present methods of applying blockage corrections in a closed rectangular high speed wind tunnel. Unpublished M.o.A. Report.

REFERENCES—*continued*

No.	*Author*	*Title, etc.*
4	W. A. Mair and H. E. Gamble	The effect of model size on measurements in the high speed tunnel. Drag of two-dimensional symmetrical aerofoils at zero incidence. A.R.C. R. & M. 2527. December, 1944.
5	E. W. E. Rogers, C. J. Berry and R. F. Cash	Tests at high subsonic speeds on a 10 per cent thick pressure-plotting aerofoil of RAE 104 section. A.R.C. R. & M. 2863. April, 1951.
6	W. P. Jones	Wind-tunnel wall interference effects on oscillating aerofoils in subsonic flow. A.R.C. R. & M. 2943. December, 1953.
7	D. E. Lehrian	Calculated derivatives for rectangular wings oscillating in compressible subsonic flow. A.R.C. R. & M. 3068. July, 1956.
8	W. P. Jones	Oscillating wings in compressible subsonic flow. A.R.C. R. & M. 2855. October, 1951.
9	W. E. A. Acum	Theory of lifting surfaces oscillating at general frequencies in a stream of high subsonic Mach number. A.R.C. 17,824. August, 1955.
	Miss D. E. Lehrian	Appendix.
10	H. C. Garner	Multhopp's subsonic lifting surface theory of wings in slow pitching oscillations. A.R.C. R. & M. 2885. July, 1952.
11	I. T. Minhinnick and D. L. Woodcock ..	Tables of aerodynamic flutter derivatives for thin wings and control surfaces in two-dimensional supersonic flow. A.R.C. C.P. 382. October, 1957.
12	Milton D. Van Dyke	Supersonic flow past oscillating airfoils including non-linear thickness effects. N.A.C.A. Report 1183. 1954.
13	A. Wylly	A second-order solution for an oscillating two-dimensional supersonic airfoil. *J. Ae. Sci.*, Vol. 19, No. 10, pp.685 to 696. 704. October, 1952.
14	W. P. Jones and S. W. Skan	Aerodynamic forces on biconvex aerofoils oscillating in a supersonic airstream. A.R.C. R. & M. 2749. August, 1951.
15	A. Chinneck, D. W. Holder and C. J. Berry	Observations of the flow round a two-dimensional aerofoil oscillating in a high-speed airstream. A.R.C. R. & M. 2931. August, 1952.

APPENDIX I

Still-Air Damping and Inertia

The assumption made in Section 2.11 that the apparatus damping was due to elastic hysteresis alone is strictly incorrect since, during the power measurement without the tunnel running, still-air damping forces were present both on the oscillating structure in the side boxes and also on the model in the tunnel working section. The correct still-air power datum should relate to the same air density and frequency of oscillation as when the tunnel is running, and should not include still-air damping on the model.

Two sets of experiments were made to determine the magnitude of the errors due to ignoring the still-air damping. In the first of these the model was removed, and each side box was sealed by a plate covering the entry to the tunnel working section. The power to oscillate the system in each box was then determined with the box evacuated to various values of pressure, and the results were plotted in the form illustrated in Fig. 45. The relationship between power and pressure is linear, and extrapolation to zero pressure gives the hysteresis power. At any pressure the power due to still-air damping is equal to the total power less that due to hysteresis, and it will be seen that this is small compared with the latter. Corrections to $-m_{\dot{\theta}}$ based on these results were in general small, but in the case of $M = 1{\cdot}61$, where the pressure change is greatest, corrections amounting to 20 per cent were obtained at the highest frequency and amplitude and rearmost axis position.

The still-air damping on the two-dimensional models might have been determined from the measurements described above and an additional set of similar measurements with the model present and the tunnel working section sealed off and made airtight. Since this would have involved a considerable amount of constructional work, the method finally adopted was to measure the apparatus damping power with a set of wooden models with chords ranging from 2 in. to 4·472 in. These models were in the form of flat plates with sharpened leading and trailing edges and were so designed that they could be fitted to the apparatus without disturbing the clamping of the torsion bars, since this had been found to alter the hysteresis damping in the system. The measurements were made at the lowest frequency of the test range (11·5 c.p.s.) in order to minimize inertial distortion effects, and measurements of power for a given amplitude of oscillation and axis position were plotted against c^4. The resulting curves, an example of which is given in Fig. 46, are linear, and the still-air power P' on the model is equal to the total power for a given chord less the value obtained by extrapolating to $c = 0$.

It may be shown by dimensional theory that the still-air power for the model takes the form

$$P' = \rho c^4 f^3 \phi\left(\frac{c^2 f}{\nu}\right), \tag{6}$$

and since it has been shown experimentally that the relation between P' and c^4 is linear for a fixed f and ρ, it follows that the function ϕ is constant for the range of c^2f/ν covered. This is the same as the range covered by variation of f with a fixed chord of 2 in. in the derivative tests, and thus the value of P' for the frequency range of these tests can be determined with the aid of (6) from the measurements at $f = 11{\cdot}5$ described above. Small changes in frequency occurred during the tests with the wooden models due to their varying size, but it was estimated that the effect on the power measurements could be ignored. Corrections to $-m_{\dot{\theta}}$ derived from these measurements turned out to be negligible.

No special tests were made to determine the still-air damping on the finite aspect ratio model, but application of the two-dimensional results discussed above indicated that the corrections were again negligible.

During the tests with the sealed side boxes, attempts were made to measure the frequency change resulting from change in pressure, with the object of evaluating corrections to $-m_\theta$ to allow for the difference in still-air inertia effects in the side boxes due to difference in air density with and without the tunnel running. However, these changes were found to be less than the normal scatter in frequency measurements, and reliable values could not be obtained. Similar considerations apply to the model, the correct datum for the stiffness measurements requiring still-air inertia effects on the model appropriate to the air density with the tunnel running. Values for the still-air inertia on the models were calculated by means of flat-plate theory, and corrections to $-m_\theta$ based on these results amounted to not more than $\frac{1}{2}$ per cent in the worst case.

APPENDIX II

Error Due to Flexure of Model

It has been assumed that in the derivative measurements described in the present paper the model has behaved as a rigid body performing pure pitching oscillations. This is only approximately true, since in general there is bound to be some flexure of the model due to aerodynamic lift forces and out-of-balance inertial reactions. These flexural displacements will give rise by coupling to aerodynamic and inertial pitching moments which will be included in the measurements and thus constitute errors in the measured derivatives.

In order to obtain some idea of the magnitude of these errors, calculations were made on the basis of the following analysis of the system used in making the measurements.

It is assumed that the system possesses two degrees of freedom, pure pitching about the axis of oscillation and pure bending of the model, there being no elastic coupling between the two displacements. Also it is assumed that apparatus and still-air damping forces may be ignored. Only the two-dimensional case has been considered, the reference section being taken at the mid-span position. It is clear, however, that the analysis applies equally well to the finite aspect ratio case if the appropriate mode of flexure is used.

The determinantal equation for the system may be written

$$\begin{vmatrix} \sigma_z - p^2 I_z + L_z + jpL_{\dot{z}}, & -p^2 P + L_\theta + jpL_{\dot{\theta}} \\ -p^2 P - M_z - jpM_{\dot{z}}, & \sigma_\theta - p^2 I_\theta - M_\theta - jp(M_{\dot{\theta}} - M_1) \end{vmatrix} = 0, \tag{7}$$

where conventional derivative notation is used, and M_1 is the driving moment applied to the system. Aerodynamic inertias are assumed included in the structural inertias I_z, I_θ, P. If no flexure were present, M_1 could be equated to $M_{\dot{\theta}}$. Due to the presence of flexure, however, an error $\delta M_{\dot{\theta}}$ exists in the damping measurement, and M_1 must satisfy the relation

$$M_1 = M_{\dot{\theta}} + \delta M_{\dot{\theta}}. \tag{8}$$

Basically the stiffness derivative M_θ is calculated from the relation

$$\sigma_\theta - p^2 I_\theta - M_\theta = 0, \tag{9}$$

where the pitching stiffness σ_θ is known from static measurements and the pitching inertia I_θ is determined by a still-air test assumed to be made at the same air density as the wind-on test. Since in general flexure is present in both cases, errors exist in the determination of both M_θ and I_θ; thus relation (9) must be written

$$\sigma_\theta - p^2(I_\theta + \delta I_\theta) - (M_\theta + \delta M_\theta) = 0. \tag{10}$$

An angular frequency p_z relating to flexure may be defined by

$$\sigma_z - p_z^2 I_z = 0, \tag{11}$$

and substitution of (8), (10), (11) in (7) then gives

$$\begin{vmatrix} \sigma_z \left(1 - \frac{p^2}{p_z^2}\right) + L_z + jpL_{\dot{z}}, & -p^2 P + L_\theta + jpL_{\dot{\theta}} \\ -p^2 P - M_z - jpM_{\dot{z}}, & p^2 \delta I_\theta + \delta M_\theta + jp\delta M_{\dot{\theta}} \end{vmatrix} = 0. \tag{12}$$

In still air at the same density (12) becomes

$$\begin{vmatrix} \sigma_z\left(1-\frac{p_0^2}{p_z^2}\right), & -p^2{}_0P \\ -p_0{}^2P, & p_0{}^2\delta I_\theta \end{vmatrix} = 0, \tag{13}$$

where the suffix 0 denotes still-air values. Elimination of δI_θ between (12) and (13) then leads to the following expression for the errors in the derivatives

$$\delta M_\theta + jp\delta M_{\dot\theta} = \frac{\{-p^2P-(M_z+jpM_{\dot z})\}\{-p^2P+(L_\theta+jpL_{\dot\theta})\}}{\sigma_z\left(1-\frac{p^2}{p_z^2}\right)+(L_z+jpL_{\dot z})} - \frac{p^2p_0{}^2P^2}{\sigma_z\left(1-\frac{p_0^2}{p_z^2}\right)}. \tag{14}$$

This may be put in the non-dimensional form

$$\delta m_\theta + j\omega\delta m_{\dot\theta} = \frac{\{-\omega^2\bar P-\kappa_1(m_z+j\omega m_{\dot z})\}\{-\omega^2\bar P+\kappa_1(l_\theta+j\omega l_{\dot\theta})\}}{\bar\sigma_z\left(1-\frac{\omega^2}{\omega_z^2}\right)+\kappa_2(l_z+j\omega l_{\dot z})} - \frac{\omega^2\omega_0{}^2\bar P^2}{\bar\sigma_z\left(1-\frac{\omega_0^2}{\omega_z^2}\right)}, \tag{15}$$

where $\bar P = P/\rho c^3 l$, $\bar\sigma_z = \sigma_z/\rho V^2 l$ and κ_1, κ_2 are integrals of the modal function $f(\eta)$ given by

$$\kappa_1 = \int_0^1 f(\eta)d\eta, \quad \kappa_2 = \int_0^1 f^2(\eta)d\eta. \tag{16}$$

In the application of (15) to the measuring system $f(\eta)$ has been taken as the static flexural mode as determined on the derivative rig for uniform spanwise loading. The same test gave σ_z, and a value for p_z was obtained by exciting flexural oscillations by means of an electromagnetic proximity exciter set up over the pitching axis. Pitching oscillations were prevented by applying the safety brakes. The product of inertia P was calculated from the known distribution of mass and the mode of distortion. From this point onwards the treatment was purely theoretical. Values for p and M were first assigned, and corresponding theoretical values for ρ and the derivative coefficients then obtained (Van Dyke's theory for supersonic speeds and flat plate for subsonic).

The calculation of δM_θ requires a value for p_0, and this was obtained by first determining I_θ from (10) and (12). For still air (10) becomes

$$\sigma_\theta - p_0{}^2(I_\theta+\delta I_\theta) = 0, \tag{17}$$

which gives a value for $p_0{}^2\delta I_\theta$ in terms of $p_0{}^2$ since I_θ is now known. Substitution in (13) then gives a quadratic in $p_0{}^2$.

Percentage errors relating to the subsonic tests are plotted in Fig. 47 against ω and M. The effects are small over the range covered, largely due to the fact that the model was mass-balanced about the axis of oscillation ($P = 0$), and it is reasonable to assume that the actual measurements will not be in very great error from this cause. In the case of the supersonic tests, however, considerable effects are indicated as shown in Figs. 48 to 51, which present curves of $-(m_\theta+\delta m_\theta)$ and $-(m_{\dot\theta}+\delta m_{\dot\theta})$

against axis position for a number of values of ω. These curves are compared with curves of $-m_\theta$ and $-m_{\dot{\theta}}$ corresponding to the case of zero flexure. In general the errors are a minimum for an axis near the mid-chord position, again due to the mass-balanced condition, and the departure from the $-m_\theta$ and $-m_{\dot{\theta}}$ curves is considerably greater for the 5 per cent thick section than for the $7\frac{1}{2}$ per cent at the higher values of ω. This might be expected in view of the smaller value of σ_z (2/5 of the value for the $7\frac{1}{2}$ per cent section) giving rise to greater flexure. The tests for the 5 per cent section were limited to the mid-chord axis position where the error is relatively small. In all cases the flexural frequency was never less than three times the pitching frequency, and thus had only a small effect on the calculated error, since it appears only in the terms $\sigma_z(1-p^2/p_z^2)$ and $\sigma_z(1-p_0^2/p_z^2)$.

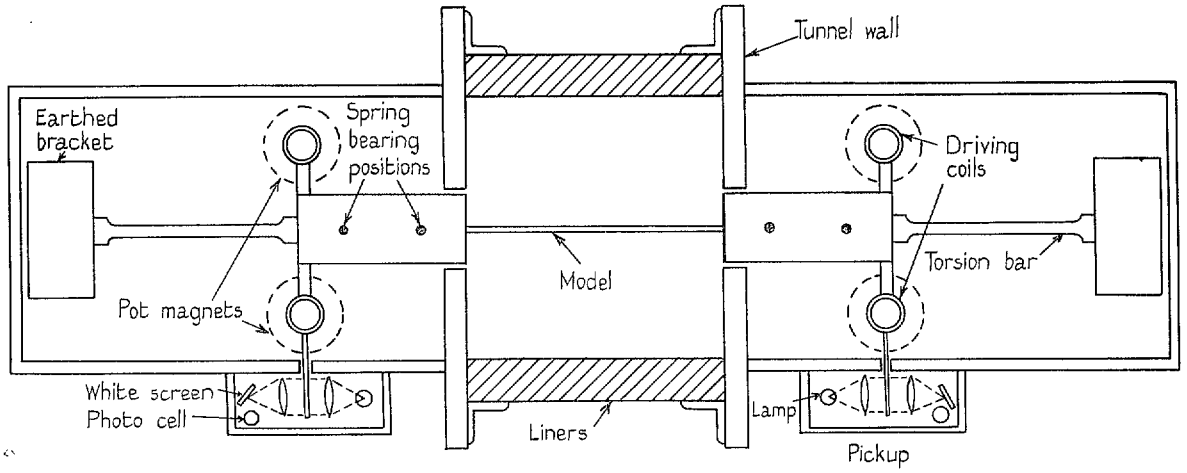

FIG. 1. Diagram of apparatus.

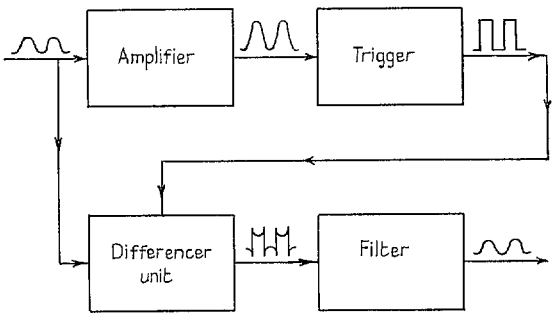

FIG. 2. Amplitude control.

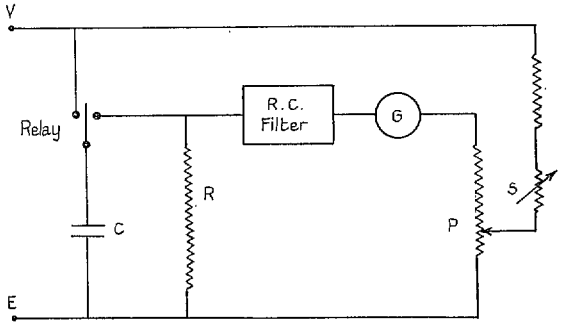

FIG. 3. Frequency meter.

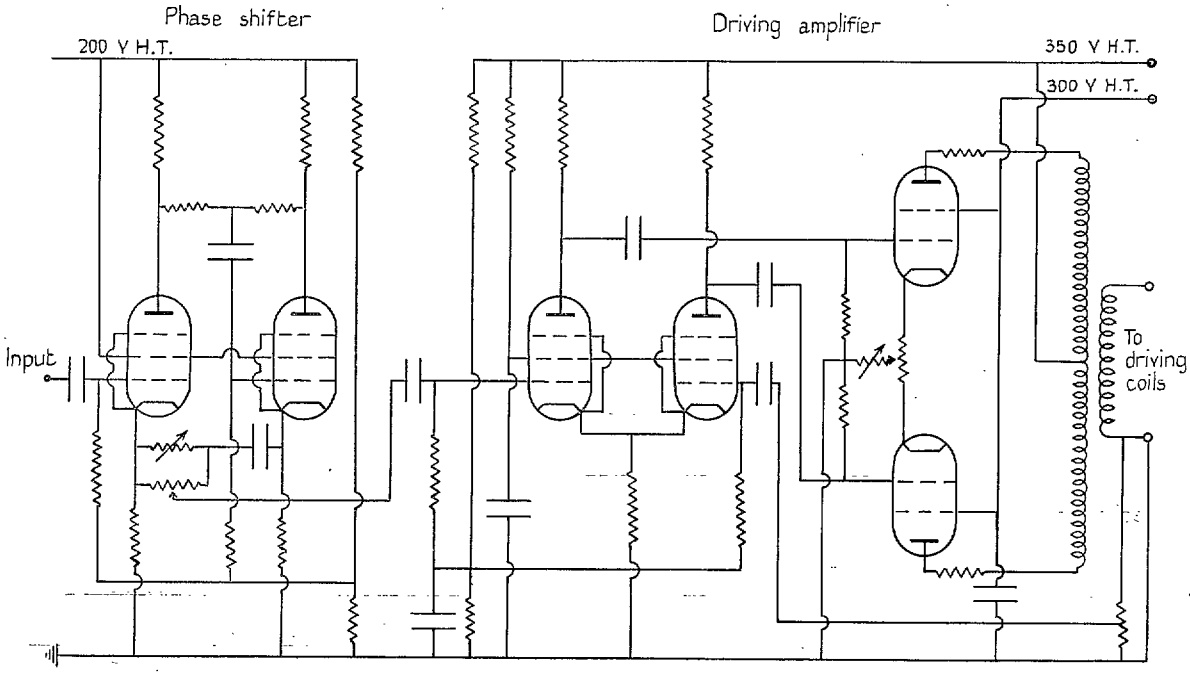

FIG. 4. Driving amplifier and phase shifter.

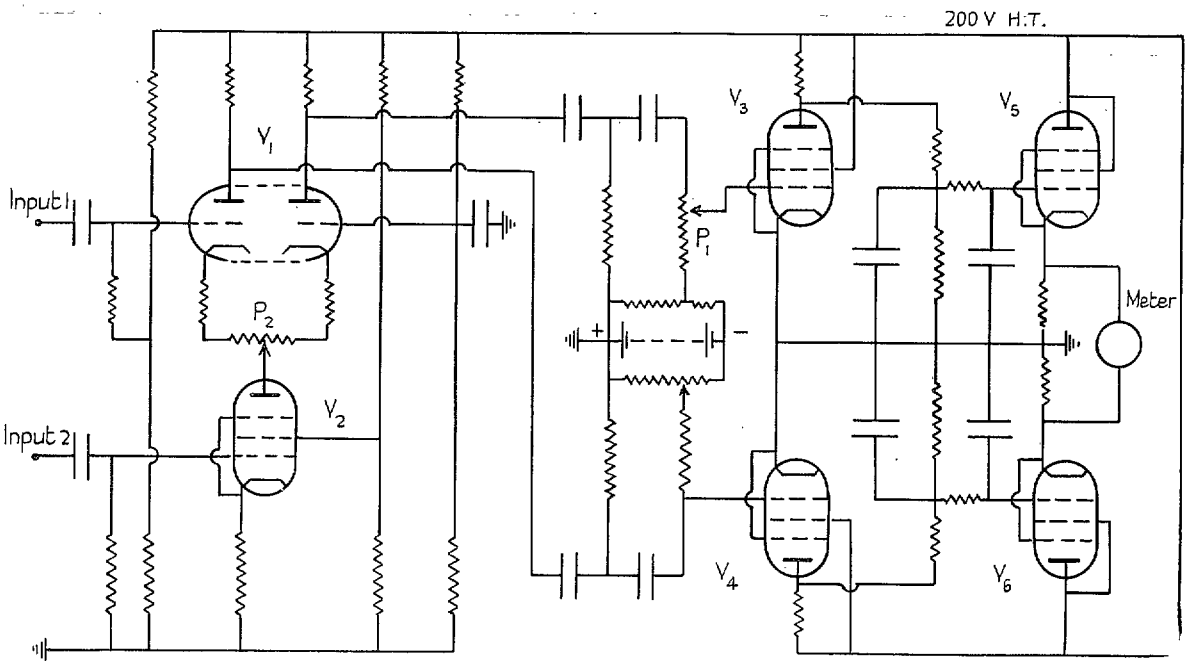

FIG. 5. Electronic wattmeter.

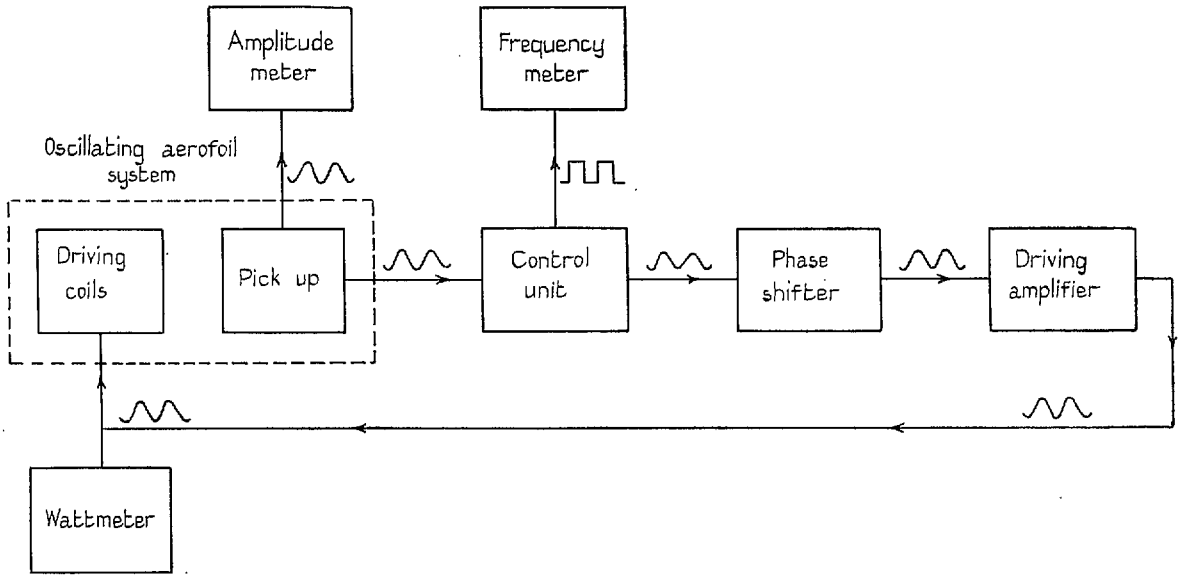

FIG. 6. Exciting and measuring circuits.

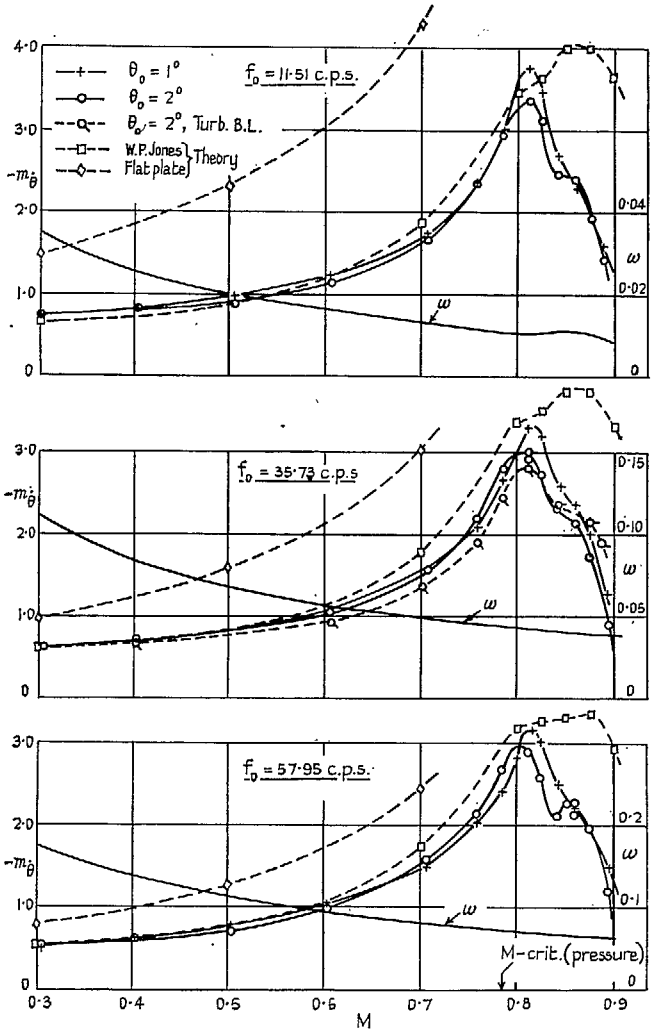

FIG. 7. Dependence of $-m_{\dot{\theta}}$ on M and ω for $\alpha = 0$ deg—RAE 104 profile, $A = \infty$.

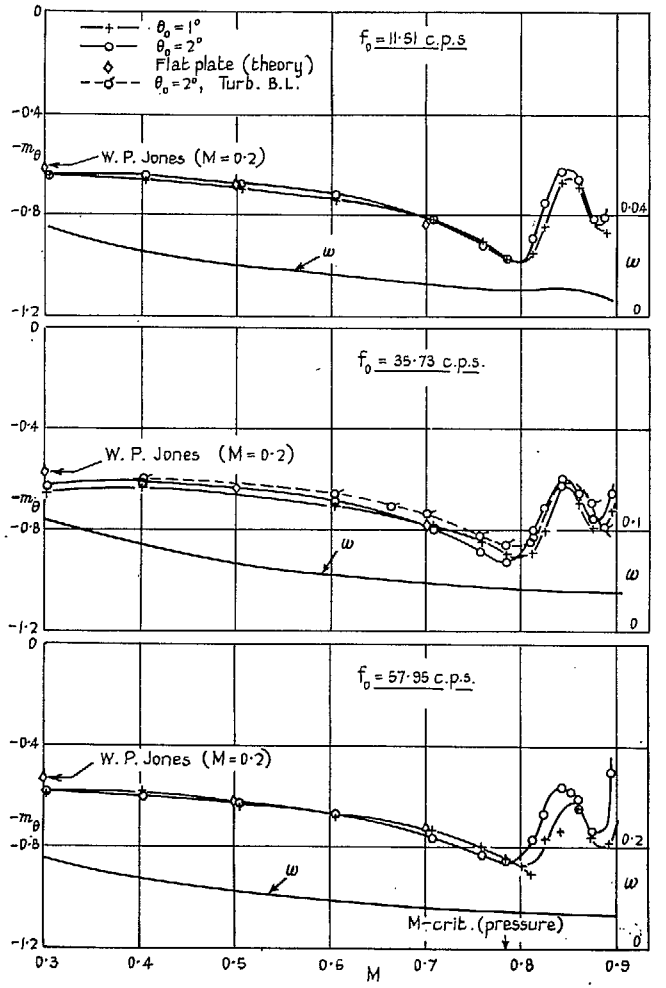

FIG. 8. Dependence of $-m_{\theta}$ on M and ω for $\alpha = 0$ deg—RAE 104 profile, $A = \infty$.

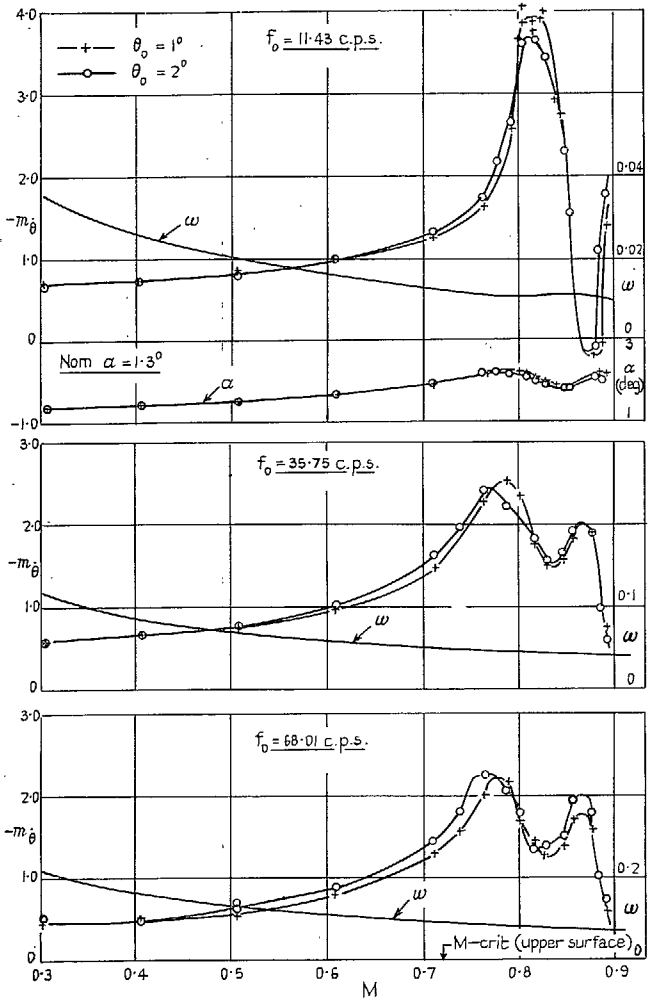

FIG. 9. Dependence of $-m_{\dot{\theta}}$ on M and ω for $\alpha = 2$ deg—RAE 104 profile, $A = \infty$.

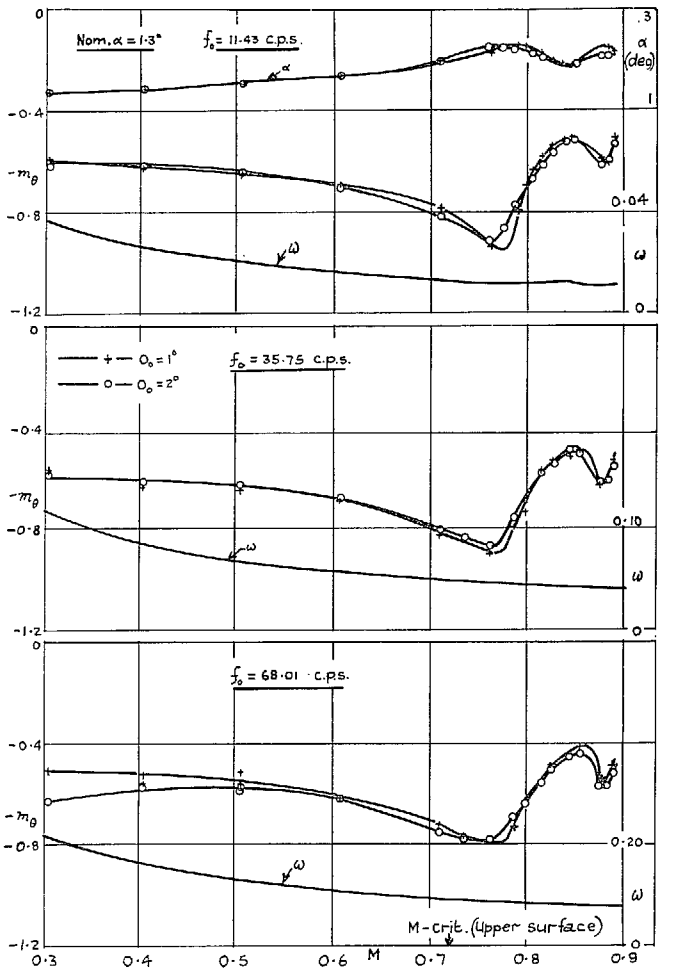

FIG. 10. Dependence of $-m_{\theta}$ on M and ω for $\alpha = 2$ deg—RAE 104 profile, $A = \infty$.

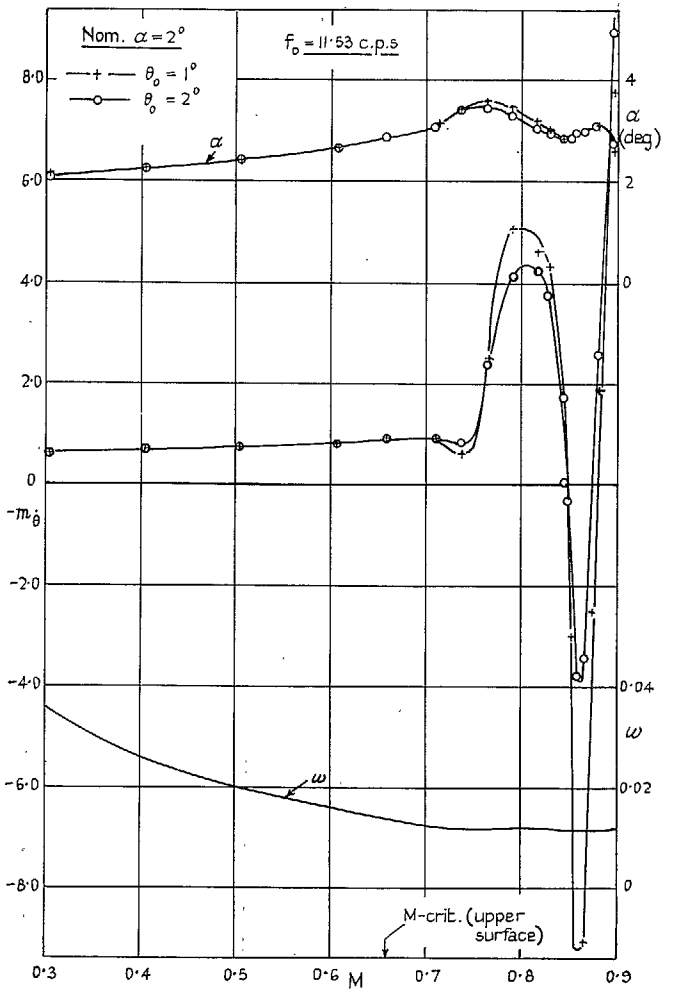

FIG. 11. Dependence of $-m_{\dot\theta}$ on M and ω for $\alpha = 3$ deg—RAE 104 profile, $A = \infty$.

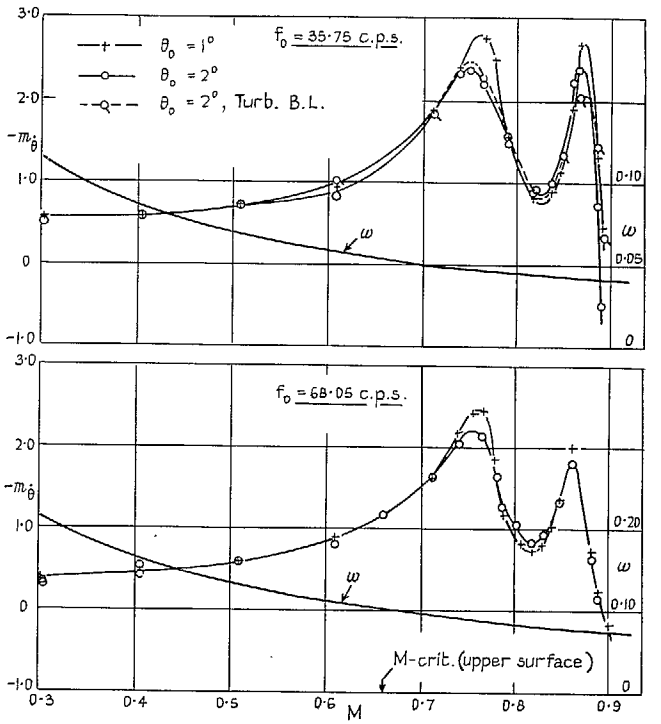

FIG. 12. Dependence of $-m_{\dot\theta}$ on ω and M for $\alpha = 3$ deg—RAE 104 profile, $A = \infty$.

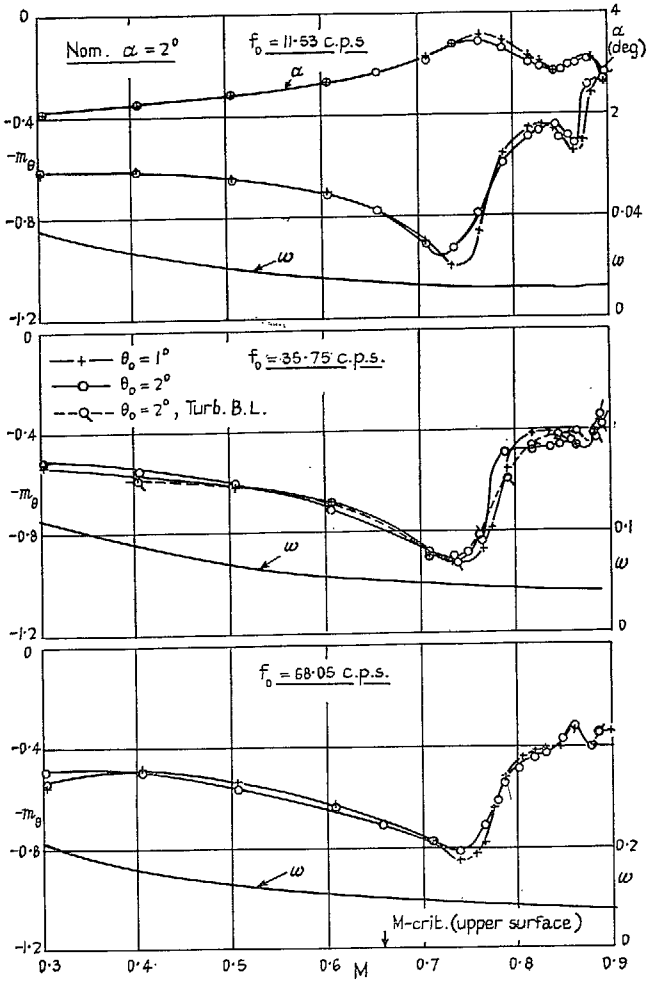

FIG. 13. Dependence of $-m_\theta$ on M and ω for $\alpha = 3$ deg—RAE 104 profile, $A = \infty$.

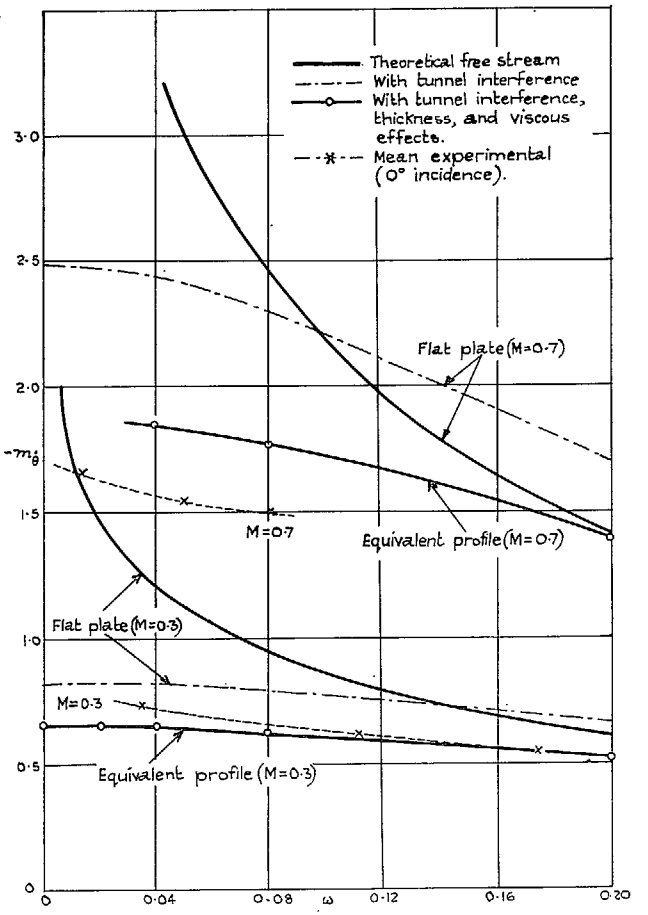

FIG. 14. Theoretical tunnel-interference, thickness and viscous effects. (Two-dimensional theory)

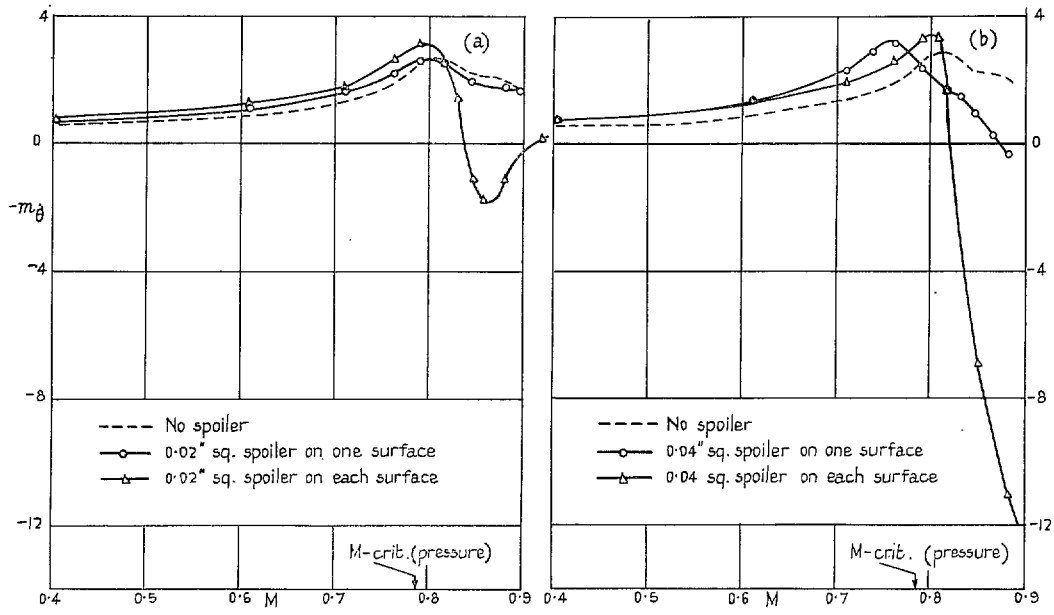

FIG. 15a and b. Effect of square-section trailing-edge spoilers on $-m_{\dot{\theta}}$ for $\alpha = 0$ deg—RAE 104 profile, $A = \infty$.

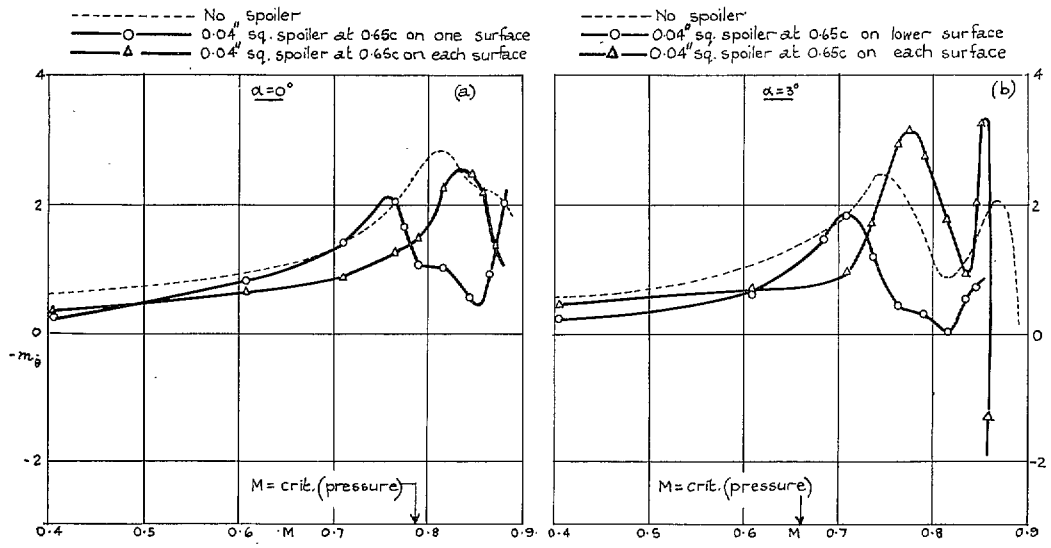

FIG. 16a and b. Effect of square-section spoilers at $0{\cdot}65c$ on $-m_{\dot{\theta}}$ for $\alpha = 0$ deg and 3 deg—RAE 104 profile, $A = \infty$.

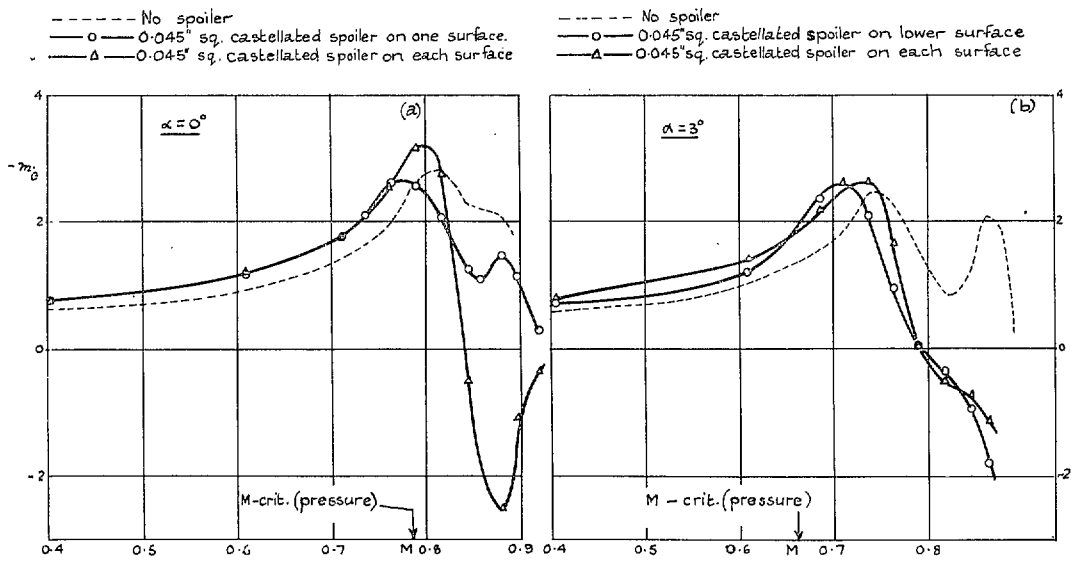

FIG. 17a and b. Effect of castellated trailing-edge spoilers on $-m_{\dot{\theta}}$ for $\alpha = 0$ deg and 3 deg—RAE 104 profile, $A = \infty$.

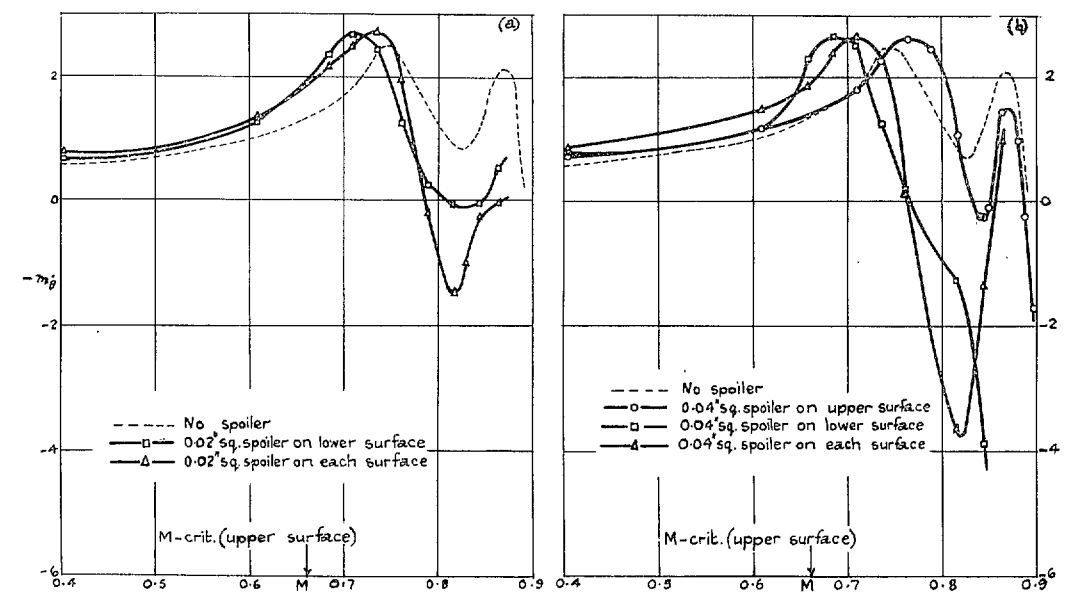

FIG. 18a and b. Effect of square-section trailing-edge spoilers on $-m_{\dot{\theta}}$ for $\alpha = 3$ deg—RAE 104 profile, $A = \infty$.

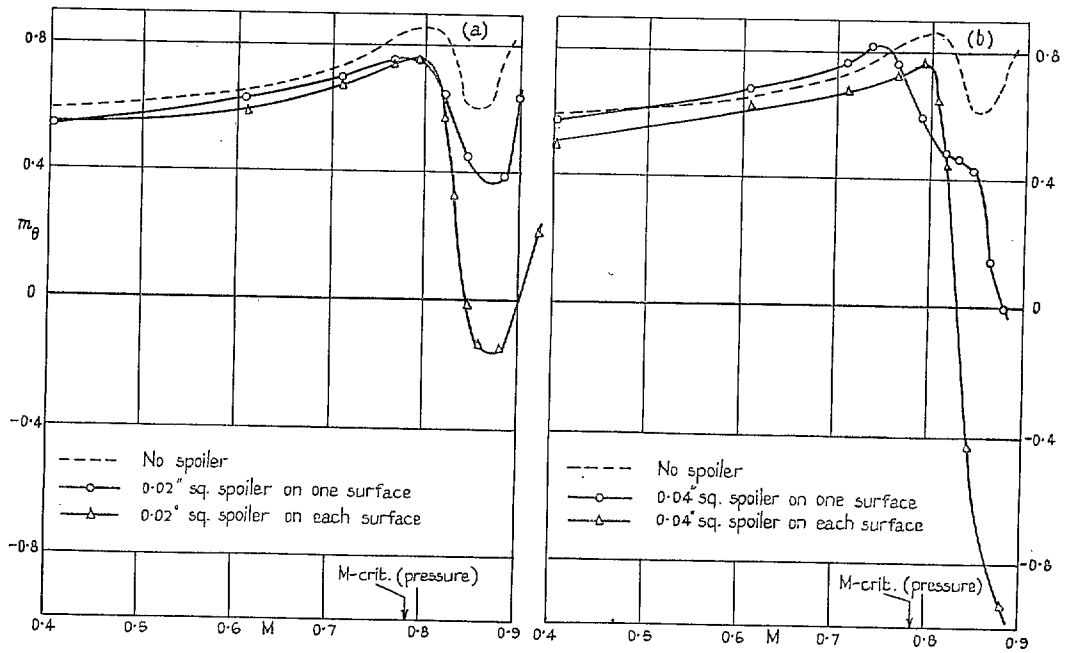

FIG. 19a and b. Effect of square-section trailing-edge spoilers on m_θ for $\alpha = 0$ deg—RAE 104 profile, $A = \infty$.

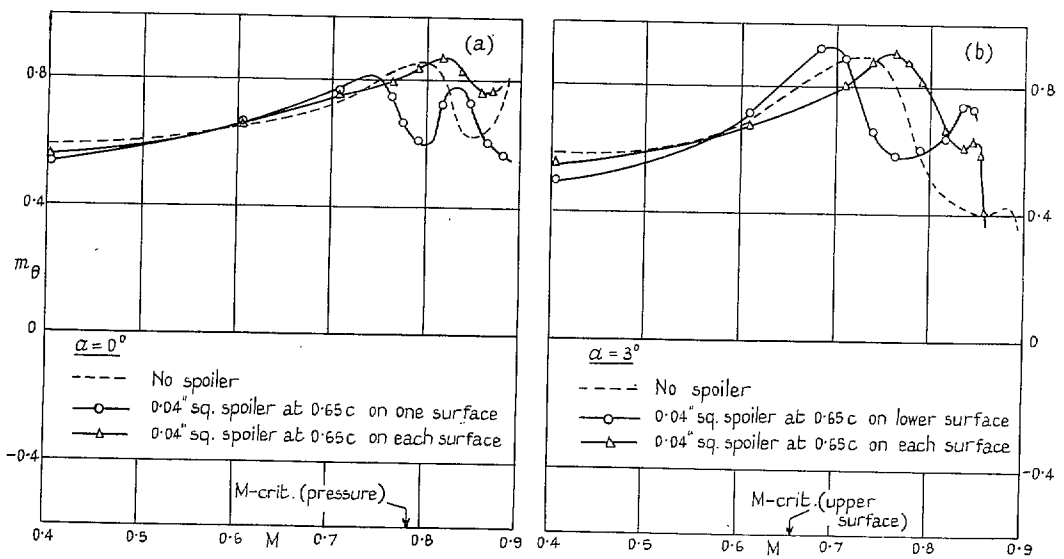

FIG. 20a and b. Effect of square-section spoilers at $0{\cdot}65c$ on m_θ for $\alpha = 0$ deg and 3 deg—RAE 104 profile, $A = \infty$.

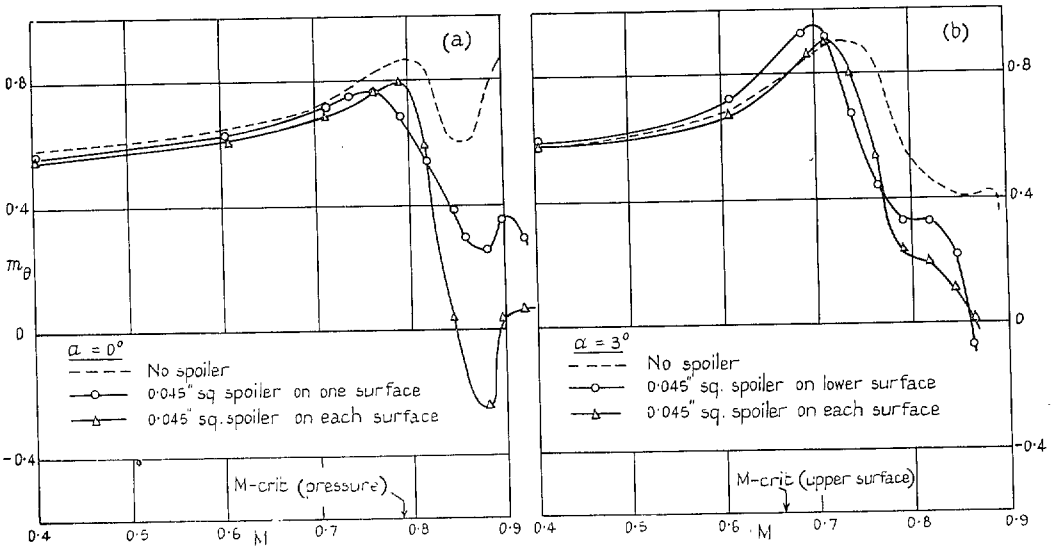

FIG. 21a and b. Effect of castellated trailing-edge spoilers on m_θ for $\alpha = 0$ deg and 3 deg—RAE'104 profile, $A = \infty$.

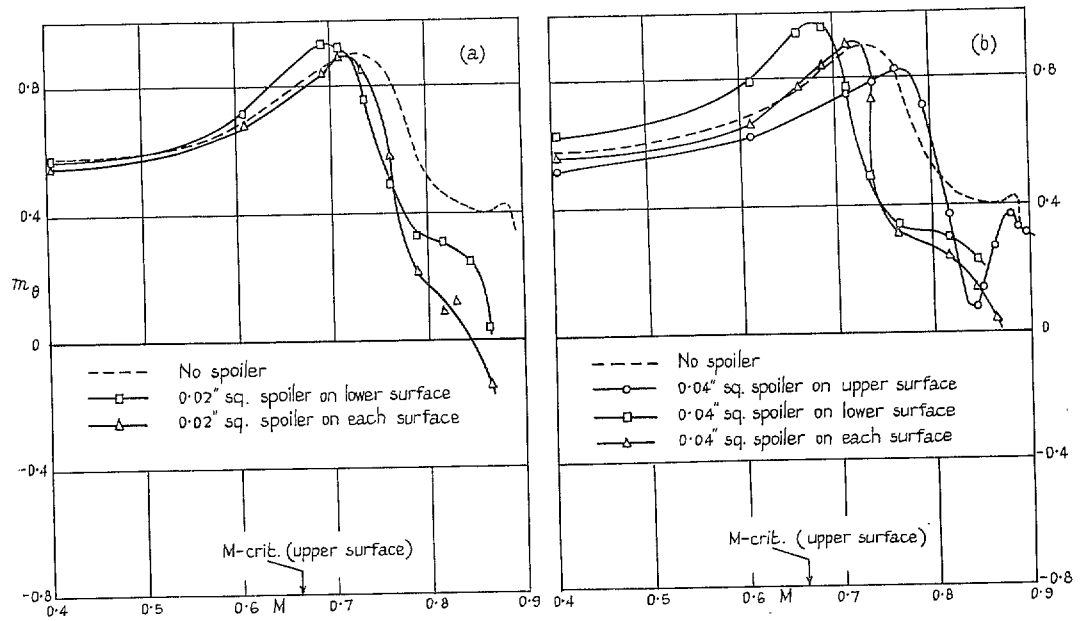

FIG. 22a and b. Effect of square-section trailing-edge spoilers on m_θ for $\alpha = 3$ deg—RAE 104 profile, $A = \infty$.

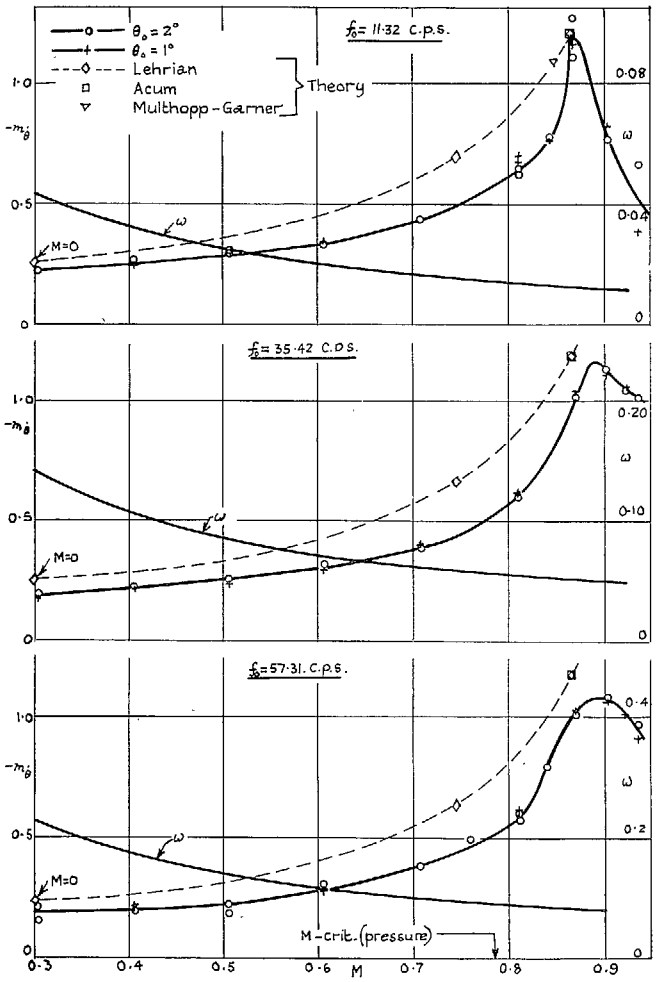

FIG. 23. Dependence of $-m_{\dot{\theta}}$ on M and ω for $\alpha = 0$ deg—RAE 104 profile, $A = 4{\cdot}0$.

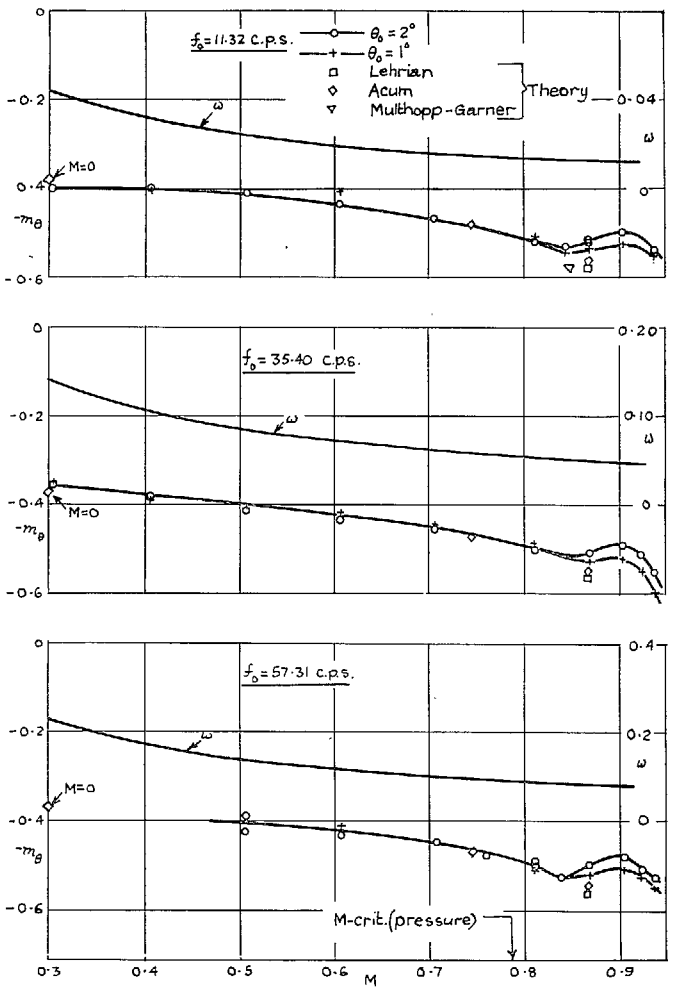

FIG. 24. Dependence of $-m_{\theta}$ on M and ω for $\alpha = 0$ deg—RAE 104 profile, $A = 4{\cdot}0$.

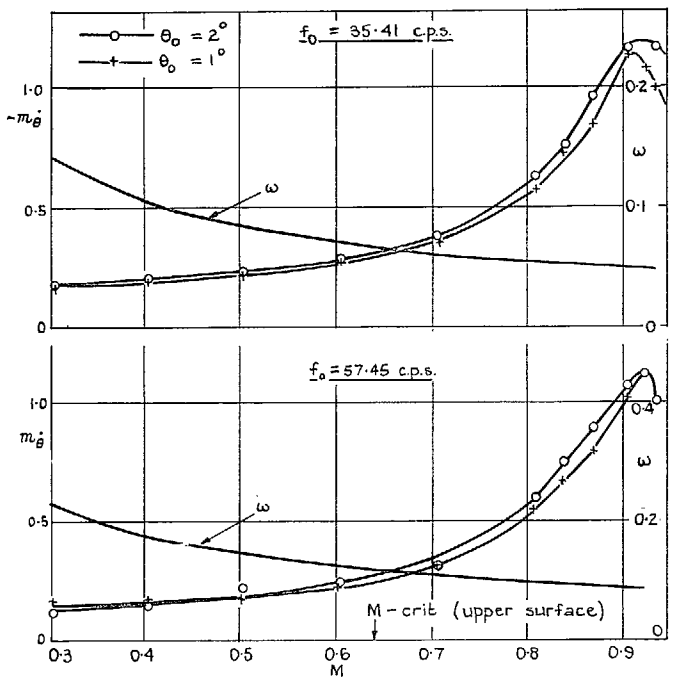

FIG. 25. Dependence of $-m_{\dot{\theta}}$ on M and ω for $\alpha = 3$ deg—RAE 104 profile, $A = 4{\cdot}0$.

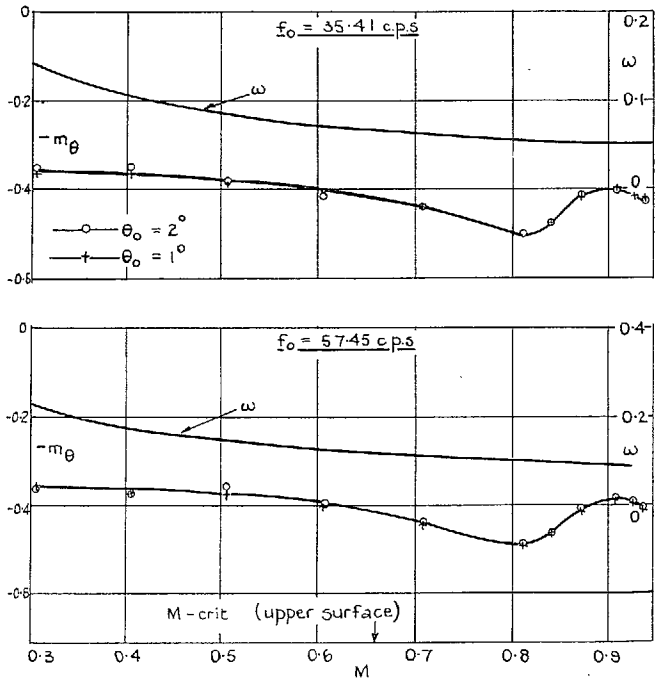

FIG. 26. Dependence of $-m_{\theta}$ on M and ω for $\alpha = 3$ deg—RAE 104 profile, $A = 4{\cdot}0$.

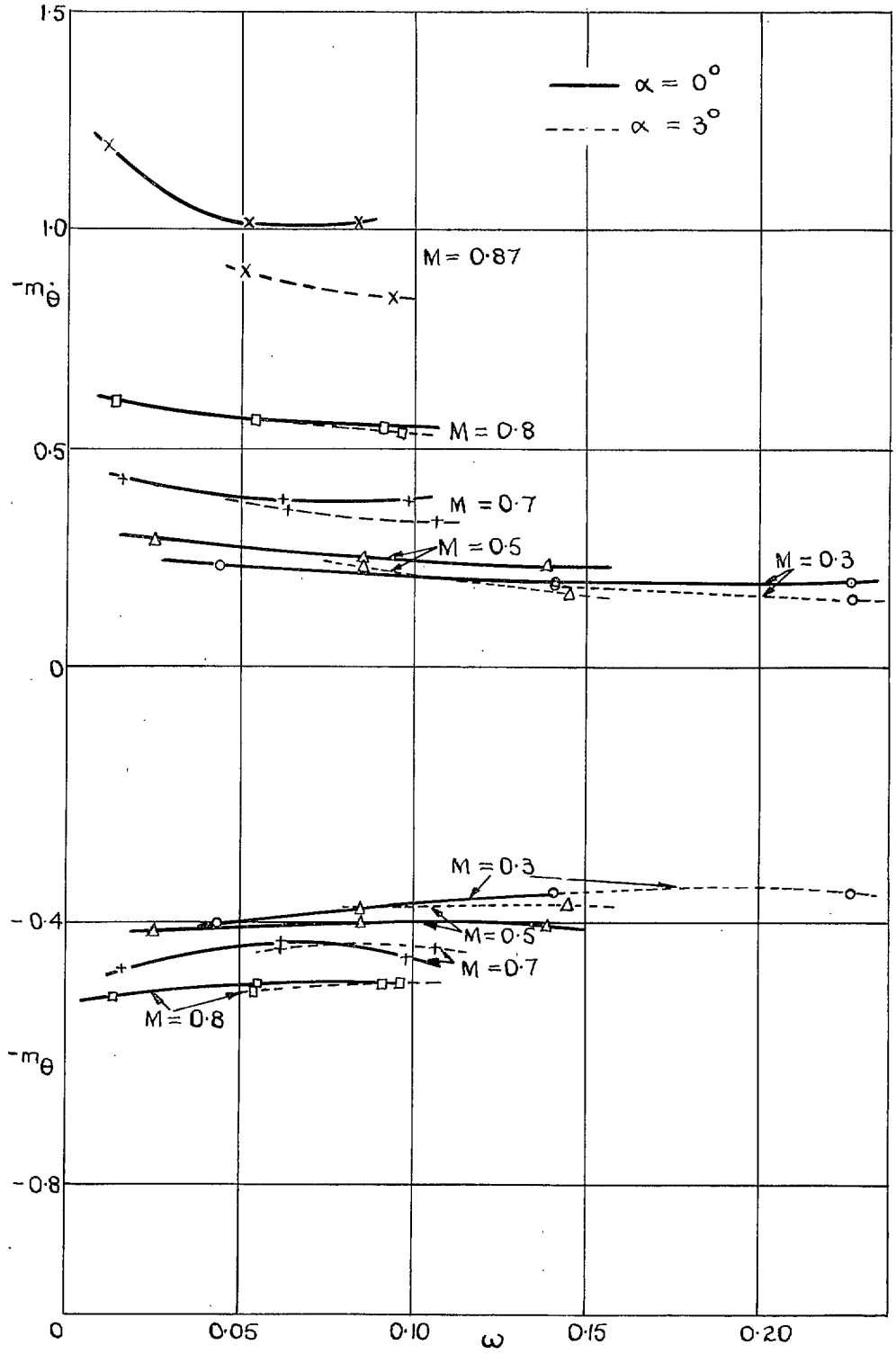

FIG. 27. Dependence of $-m_{\dot{\theta}}$ and $-m_{\theta}$ on ω—RAE 104 profile, $A = 4{\cdot}0$.

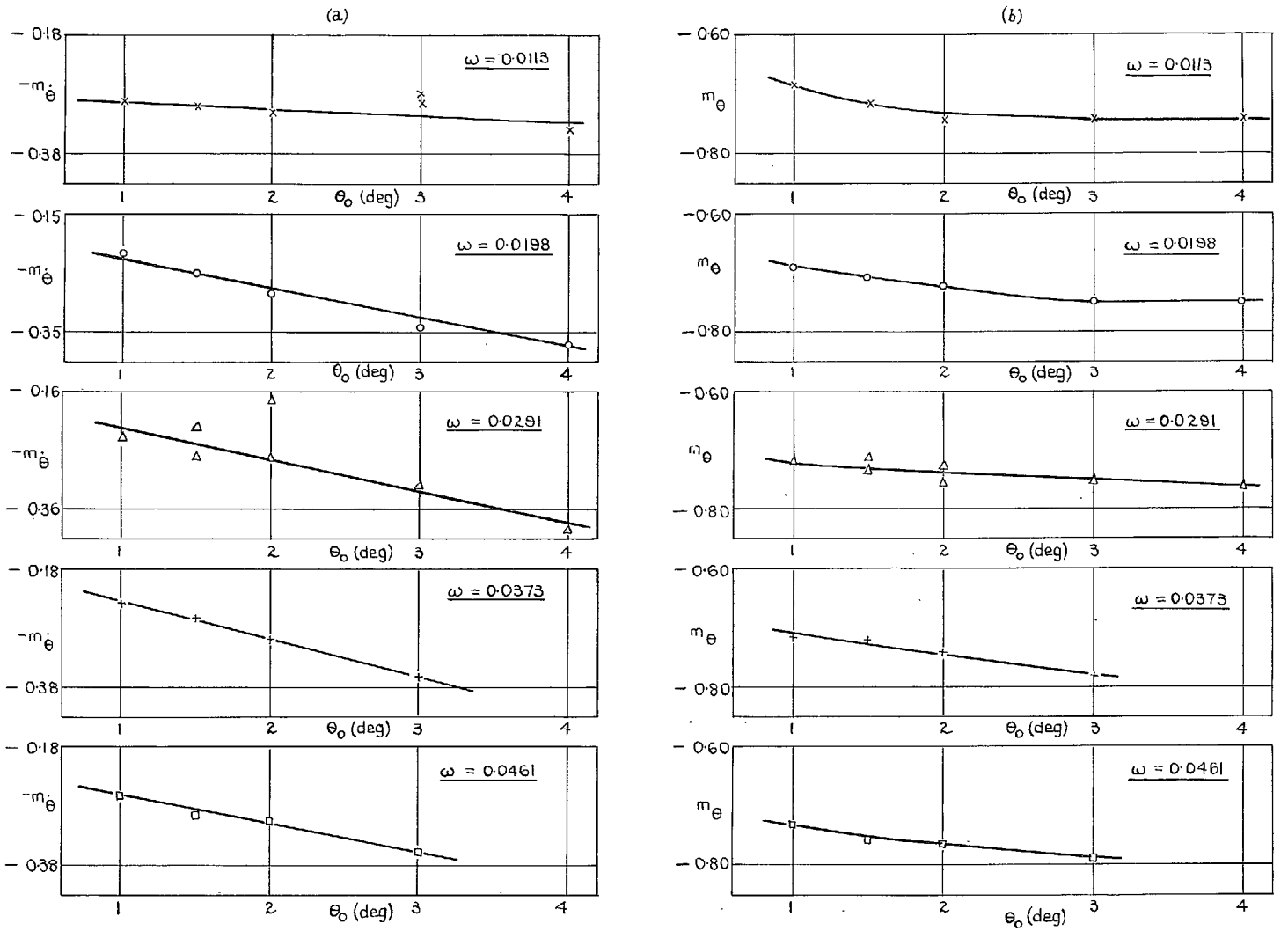

FIG. 28a and b. Dependence of $-m_{\dot\theta}$ and m_θ on θ_0 and ω—$7\frac{1}{2}$ per cent biconvex profile, $M = 1{\cdot}42$. Axis at leading edge.

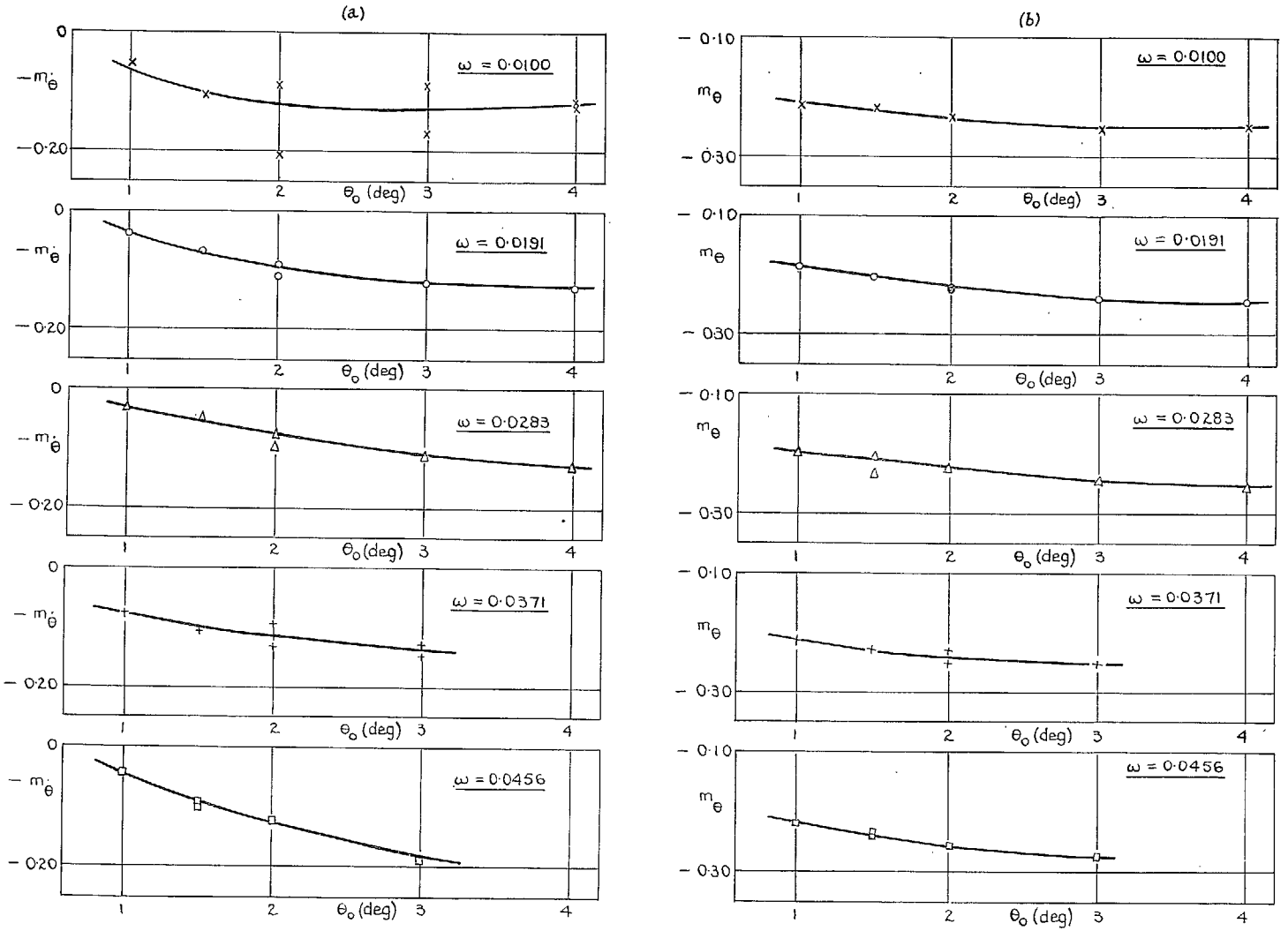

FIG. 29a and b. Dependence of $-m_{\dot\theta}$ and m_θ on θ_0 and ω—$7\frac{1}{2}$ per cent biconvex profile, $M = 1{\cdot}42$. Axis at $0{\cdot}25c$.

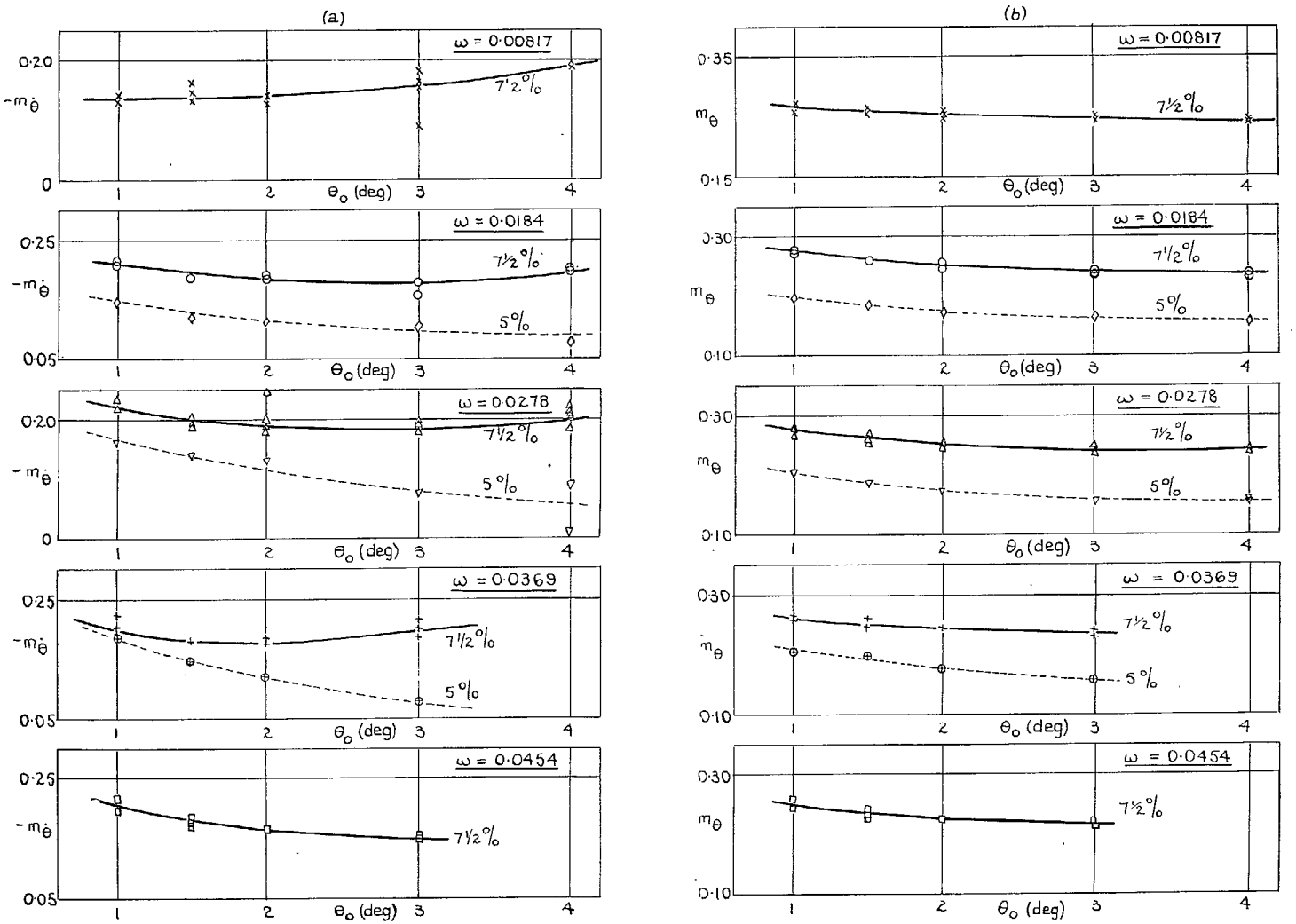

FIG. 30a and b. Dependence of $-m_{\dot\theta}$ and m_θ on θ_0 and ω—$7\frac{1}{2}$ per cent and 5 per cent biconvex profiles, $M = 1{\cdot}42$. Axis at $0{\cdot}5c$.

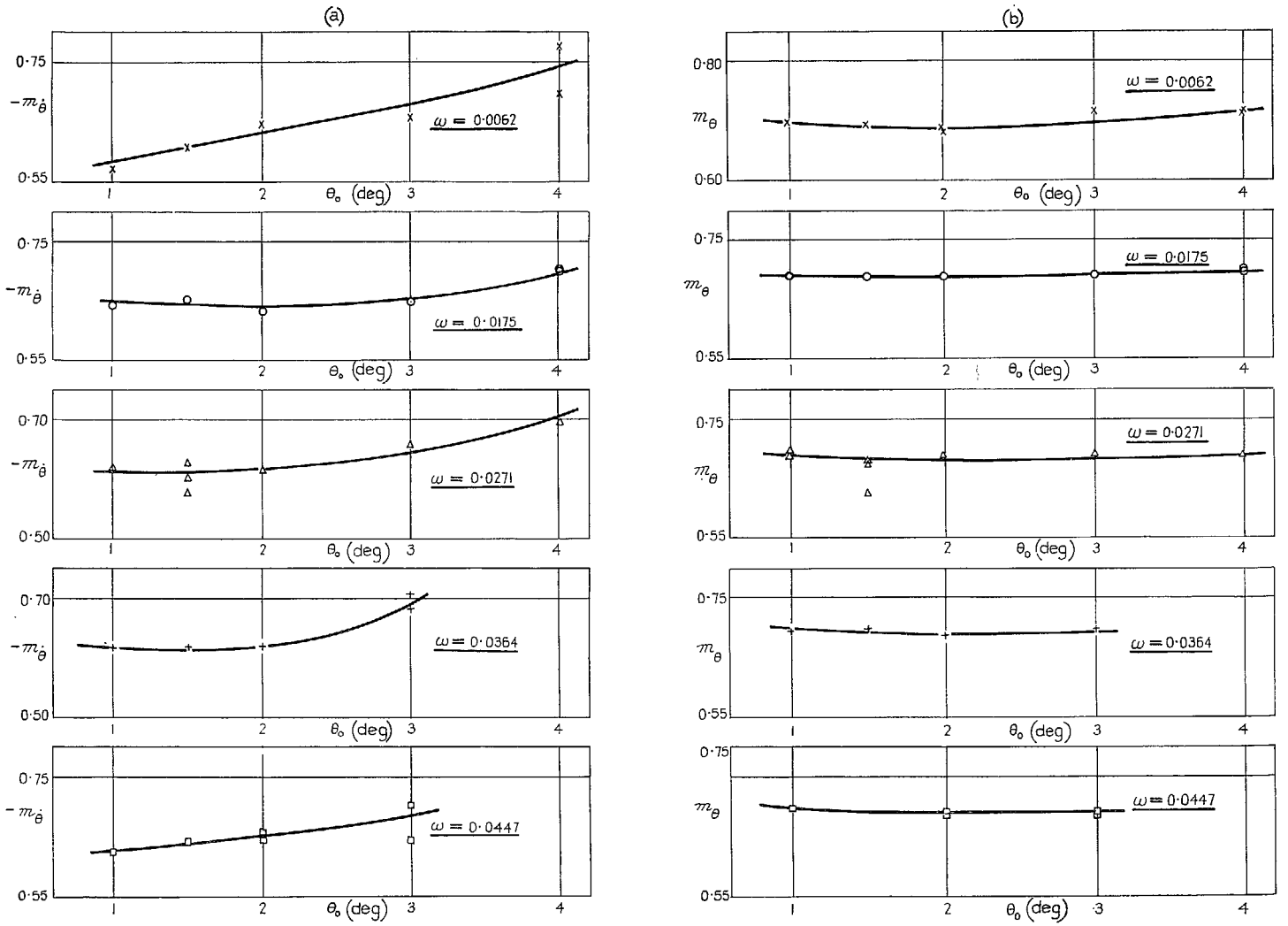

FIG. 31a and b. Dependence of $-m_{\dot\theta}$ and m_θ on θ_0 and ω—$7\frac{1}{2}$ per cent biconvex profile, $M = 1{\cdot}42$. Axis at $0{\cdot}75c$.

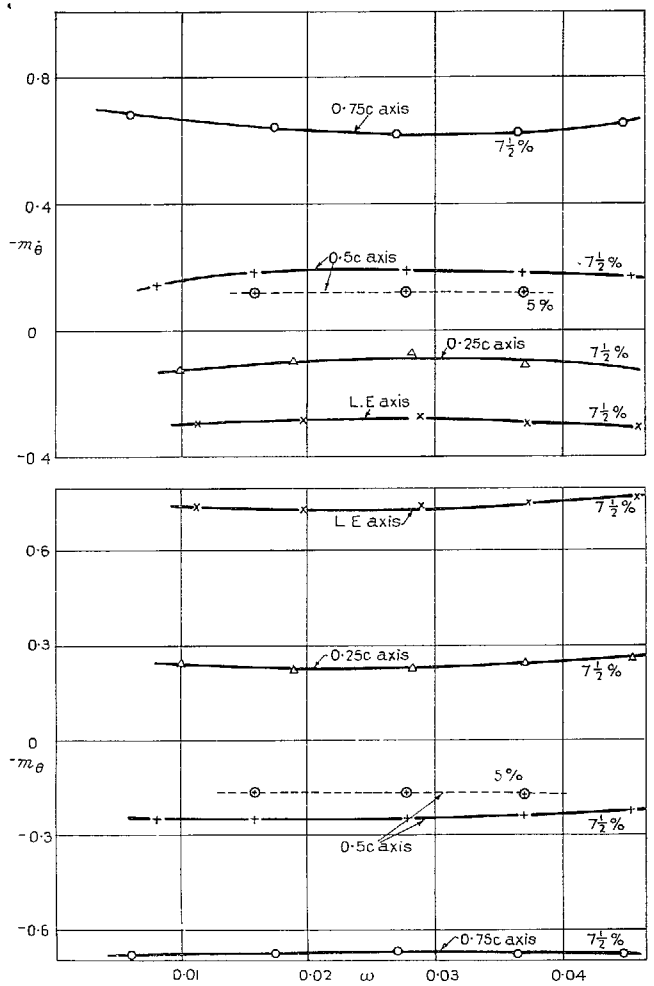

FIG. 32. Dependence of $-m_{\dot\theta}$ and $-m_\theta$ on ω for $7\frac{1}{2}$ per cent and 5 per cent biconvex profiles—$\theta_0 = 2$ deg, $M = 1{\cdot}42$.

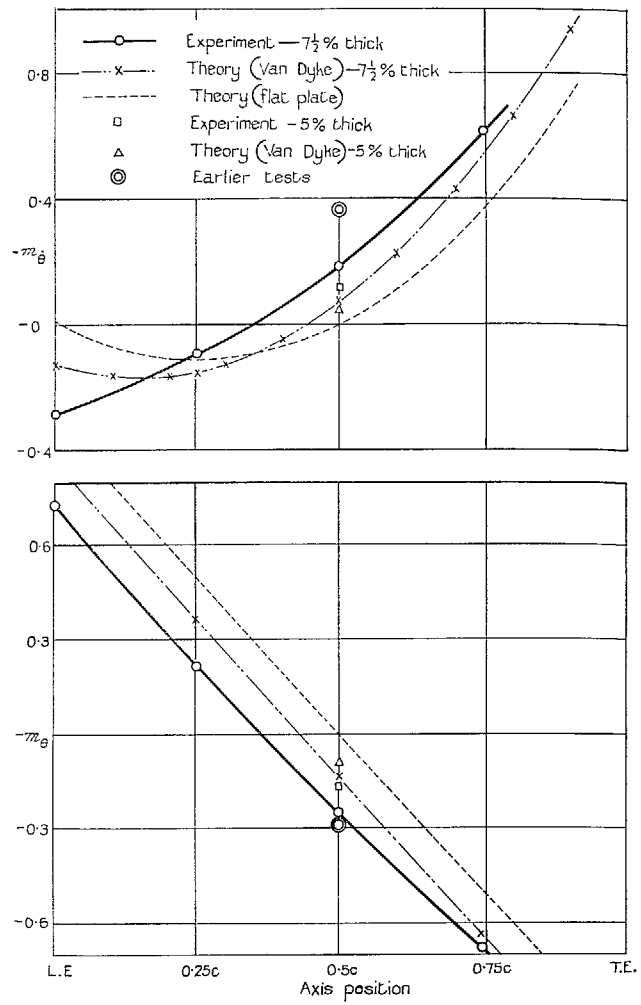

FIG. 33. Dependence of $-m_{\dot\theta}$ and $-m_\theta$ on axis position—$\theta_0 = 2$ deg, $\omega = 0{\cdot}025$, $M = 1{\cdot}42$.

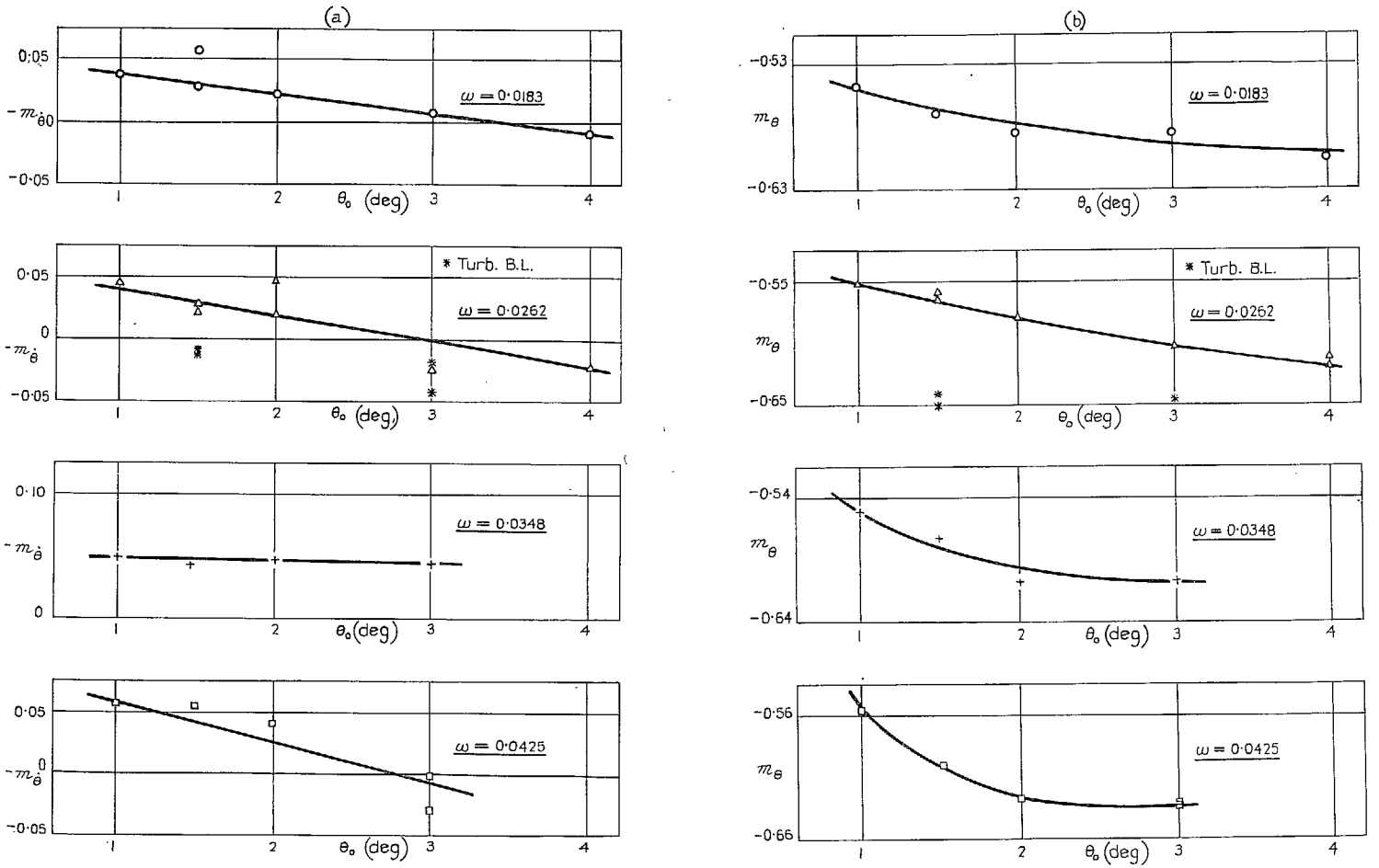

FIG. 34a and b. Dependence of $-m_{\dot\theta}$ and m_θ on θ_0 and ω—$7\frac{1}{2}$ per cent biconvex profile, $M = 1{\cdot}61$. Axis at leading edge.

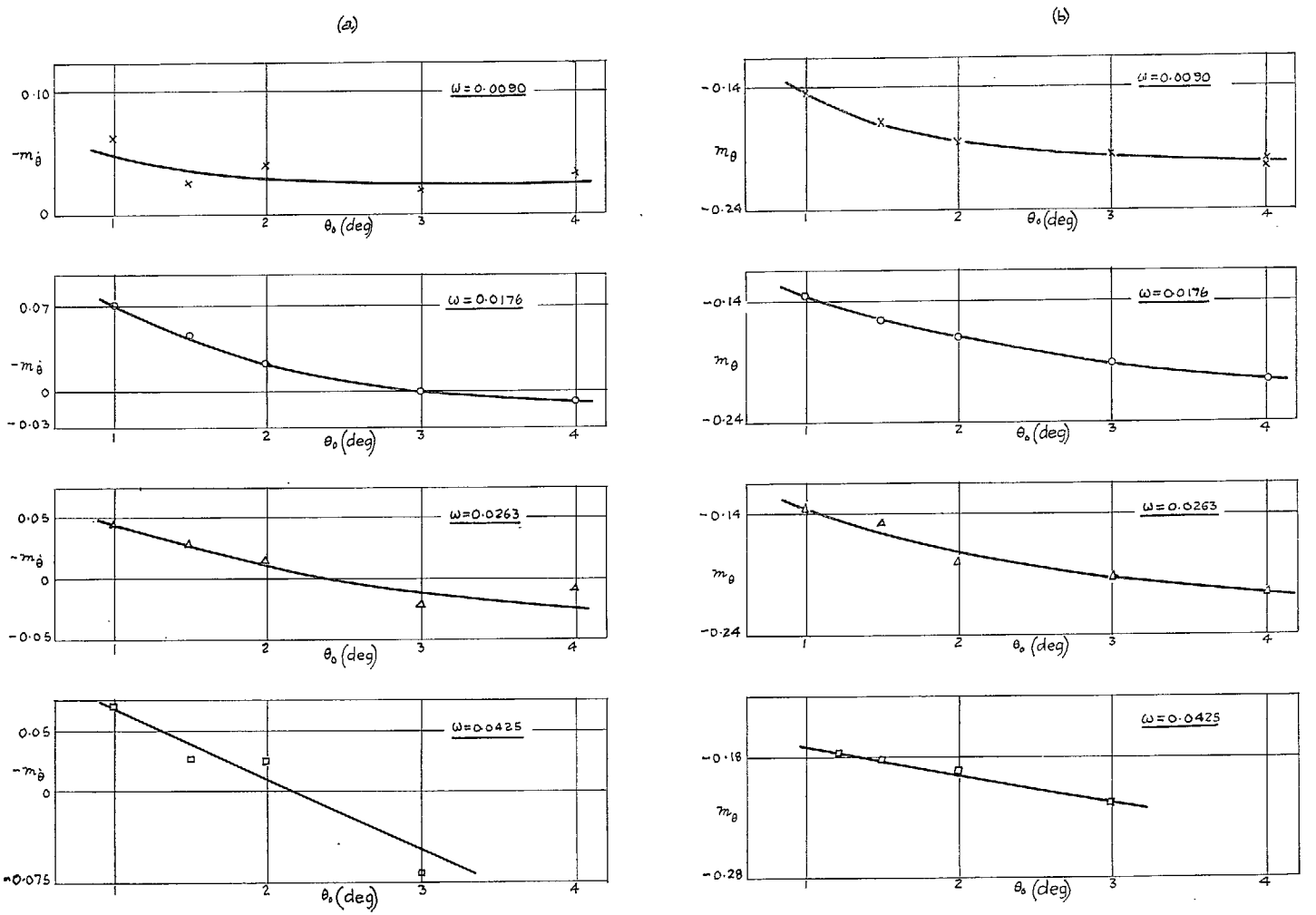

FIG. 35a and b. Dependence of $-m_{\dot\theta}$ and m_θ on θ_0 and ω—$7\frac{1}{2}$ per cent biconvex profile, $M = 1{\cdot}61$. Axis at $0{\cdot}25c$.

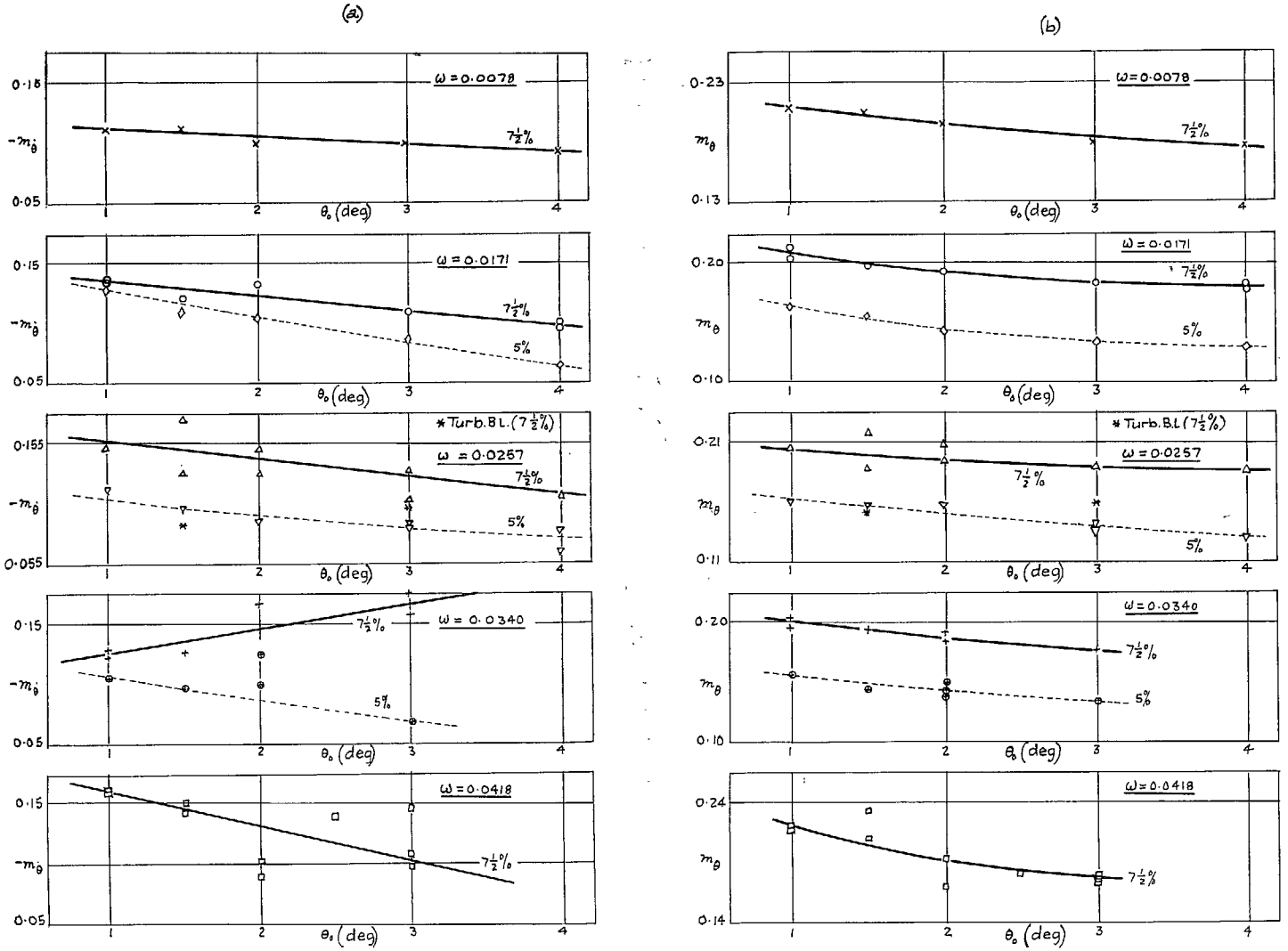

FIG. 36a and b. Dependence of $-m_{\dot{\theta}}$ and m_θ on θ_0 and ω—$7\frac{1}{2}$ per cent and 5 per cent biconvex profile, $M = 1{\cdot}61$. Axis at $0{\cdot}5c$.

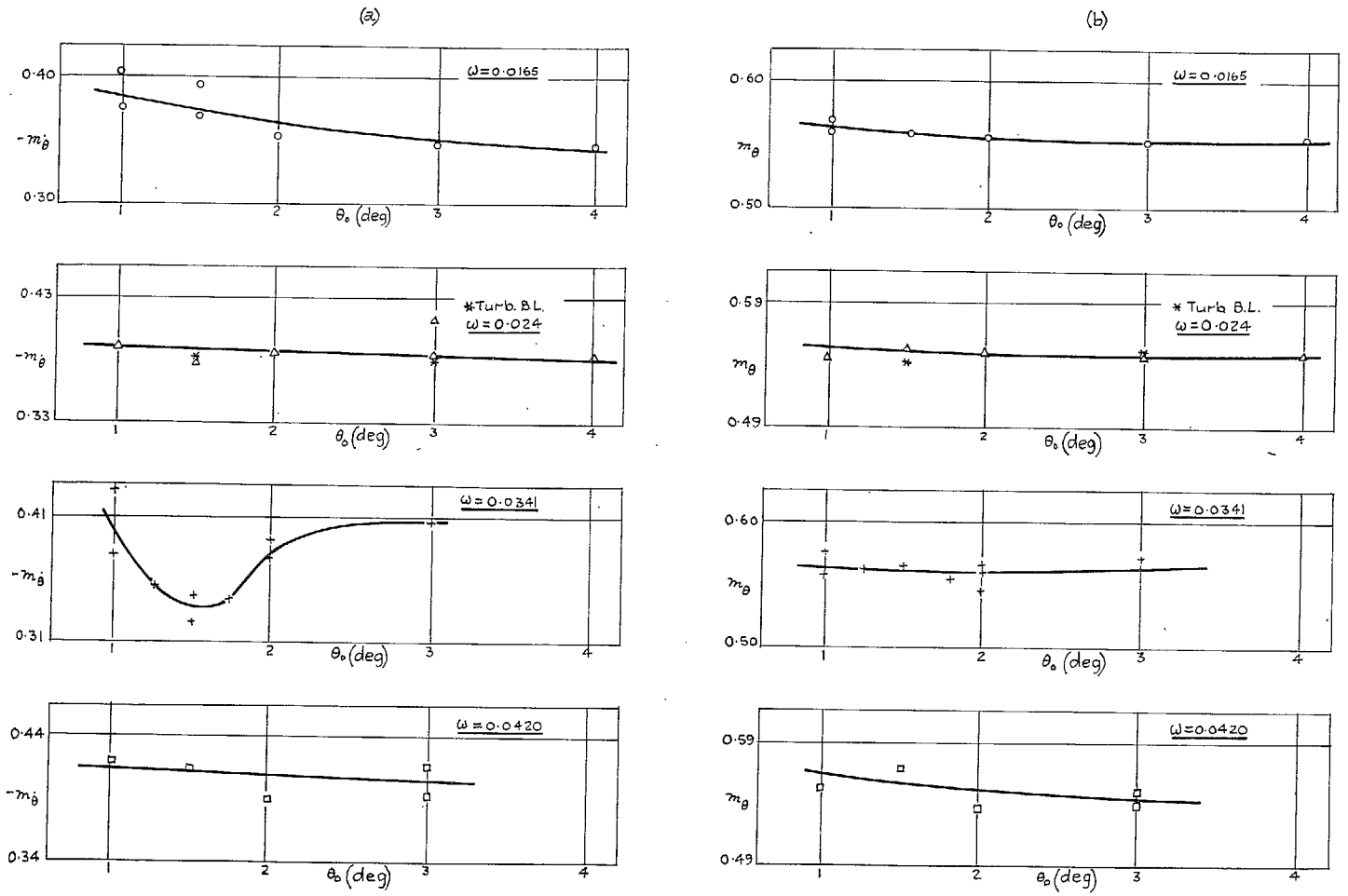

FIG. 37a and b. Dependence of $-m_{\dot\theta}$ and m_θ on θ_0 and ω—$7\frac{1}{2}$ per cent biconvex profile, $M = 1{\cdot}61$. Axis at $0{\cdot}75c$.

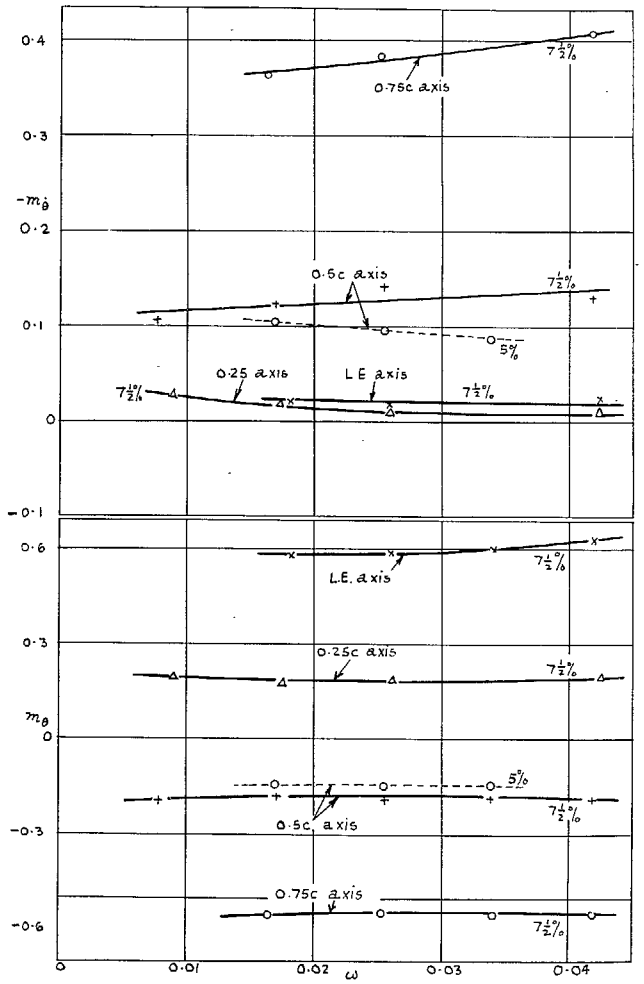

FIG. 38. Dependence of $-m_{\dot\theta}$ and $-m_\theta$ on ω for $7\frac{1}{2}$ per cent and 5 per cent biconvex profiles—$\theta_o = 2$ deg, $M = 1{\cdot}61$.

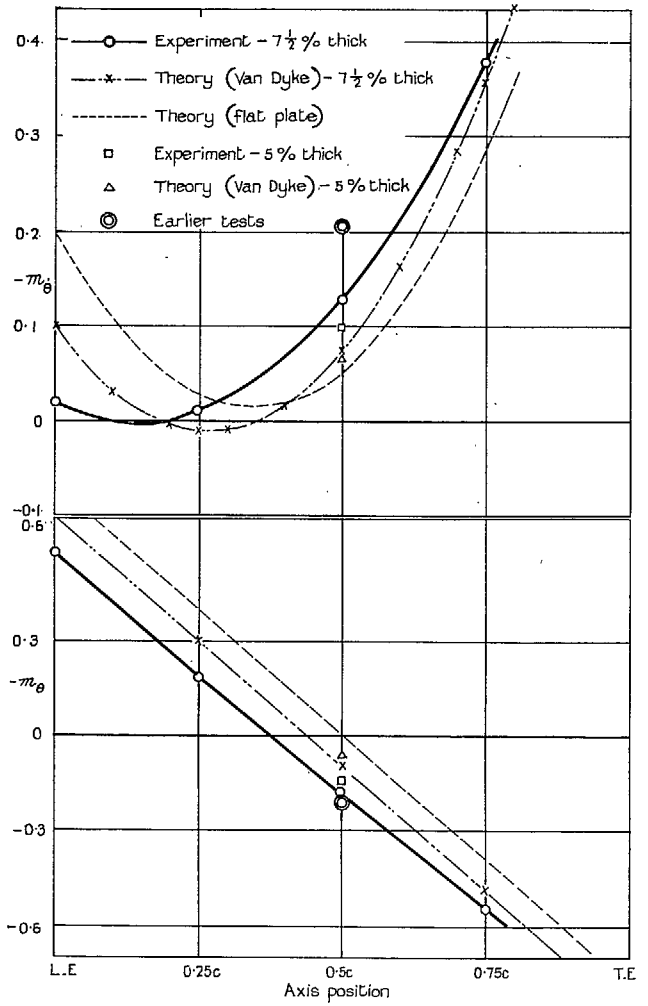

FIG. 39. Dependence of $-m_{\dot\theta}$ and $-m_\theta$ on axis position—$\theta_0 = 2$ deg, $\omega = 0{\cdot}025$, $M = 1{\cdot}61$.

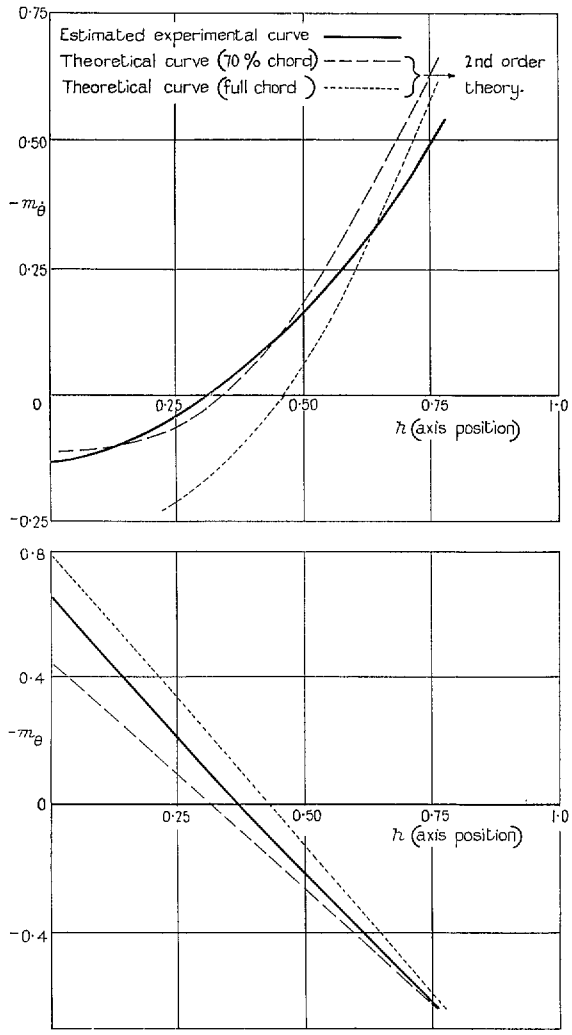

FIG. 40. Comparison with theory for 70 per cent chord—$7\frac{1}{2}$ per cent biconvex profile, $\theta_0 = 2$ deg, $\omega = 0{\cdot}025$, $M = 1{\cdot}5$.

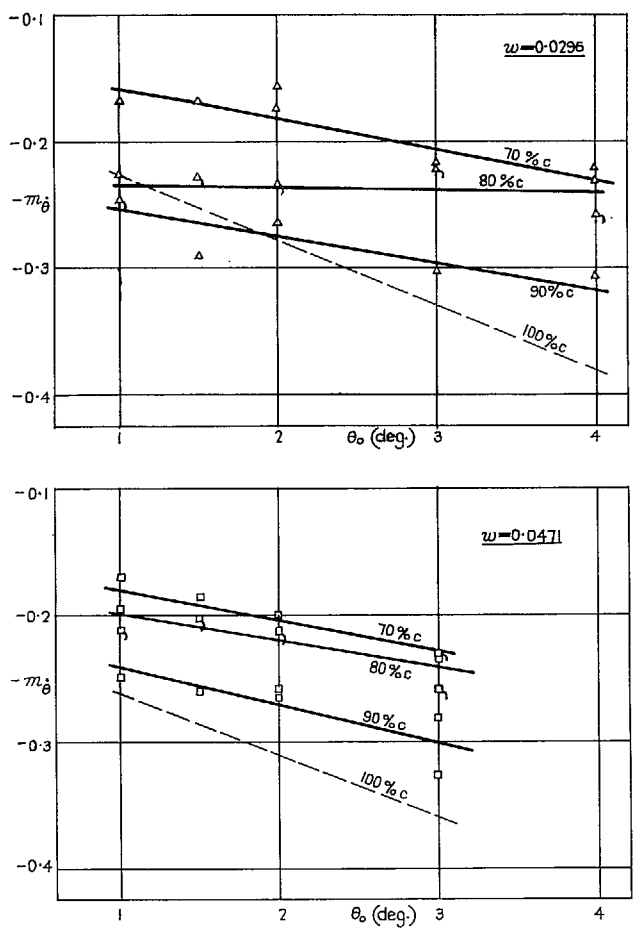

FIG. 41. Effect on $-m_{\dot{\theta}}$ of cutting off trailing edge—$7\frac{1}{2}$ per cent biconvex profile, $M = 1{\cdot}42$. Axis at leading edge.

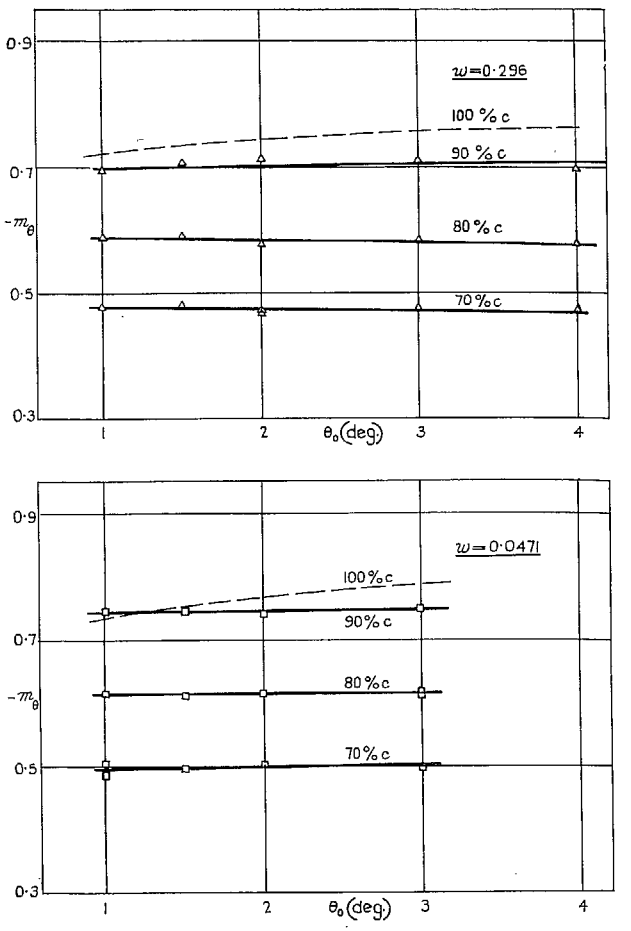

FIG. 42. Effect on $-m_{\theta}$ of cutting off trailing edge—$7\frac{1}{2}$ per cent biconvex profile, $M = 1{\cdot}42$. Axis at leading edge.

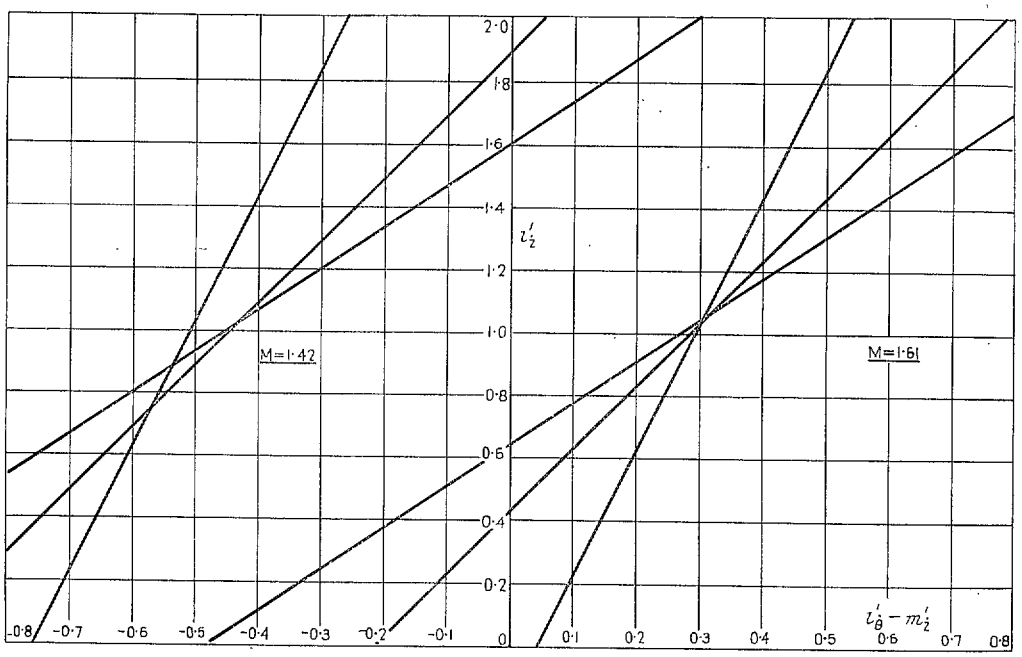

FIG. 43. Error triangles for determination of l_z and $l_\theta - m_z$—7½ per cent biconvex profile, $\theta_o = 2$ deg, $\omega = 0{\cdot}025$.

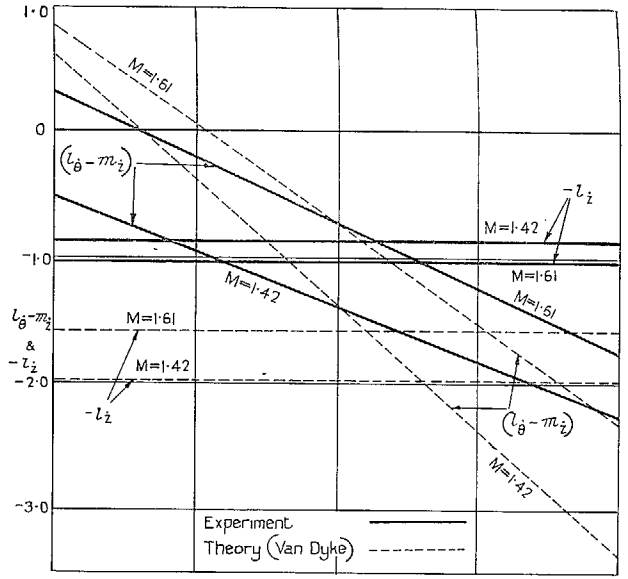

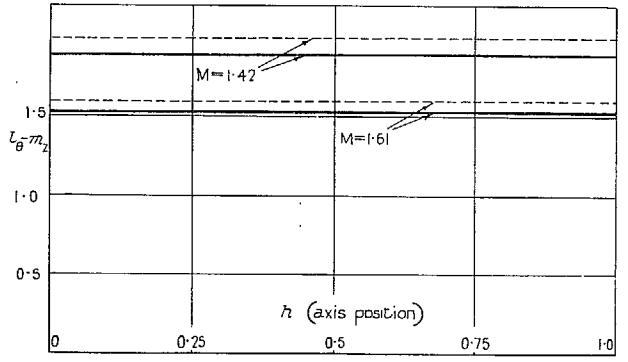

FIG. 44. Dependence of $(l_{\dot\theta} - m_{\dot z})$, $-l_z$ and $(l_\theta - m_z)$ on axis position—$7\frac{1}{2}$ per cent biconvex profile, $\theta_0 = 2$ deg, $\omega = 0{\cdot}025$.

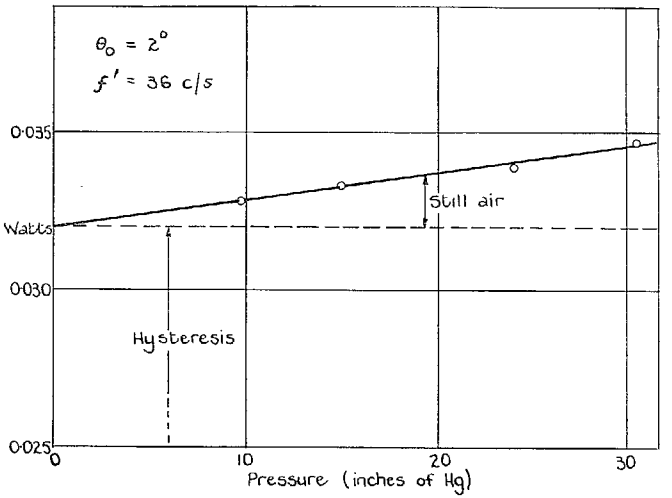

FIG. 45. Apparatus damping in side box No. 1.

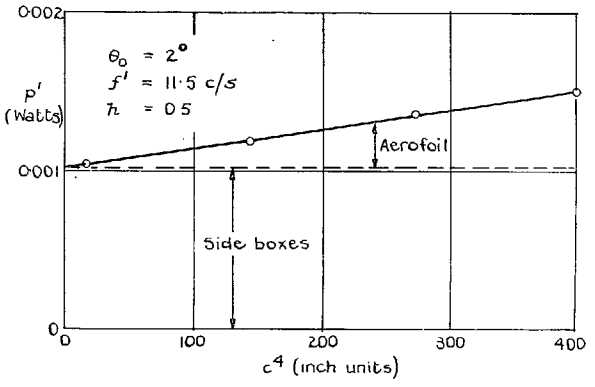

FIG. 46. Two-dimensional still-air damping.

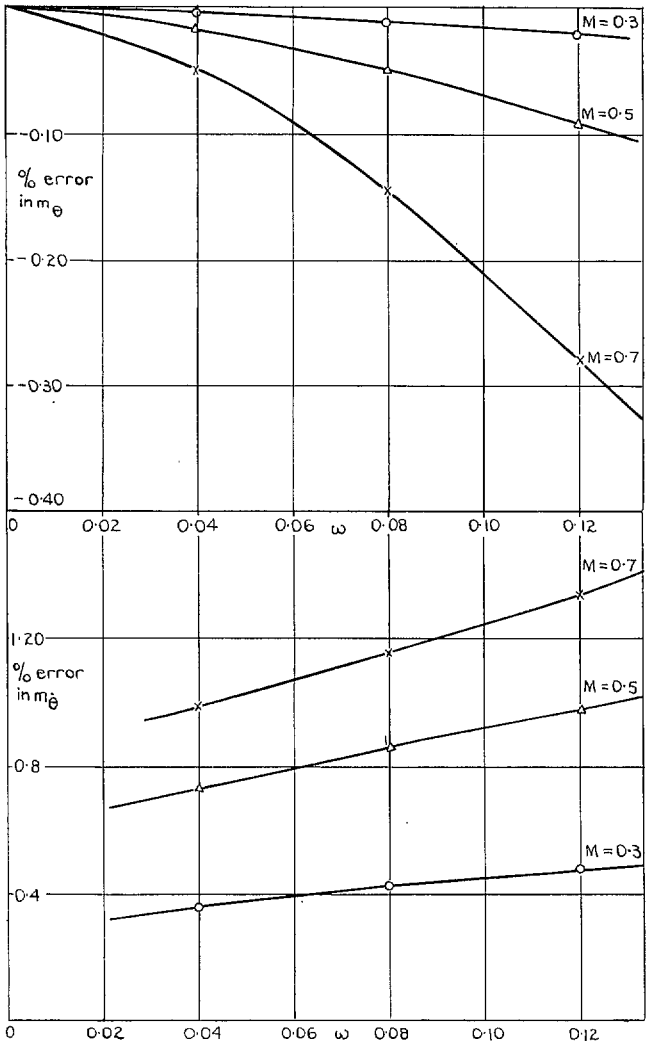

FIG. 47. Percentage error due to flexure—RAE 104 model, $h = 0 \cdot 445$.

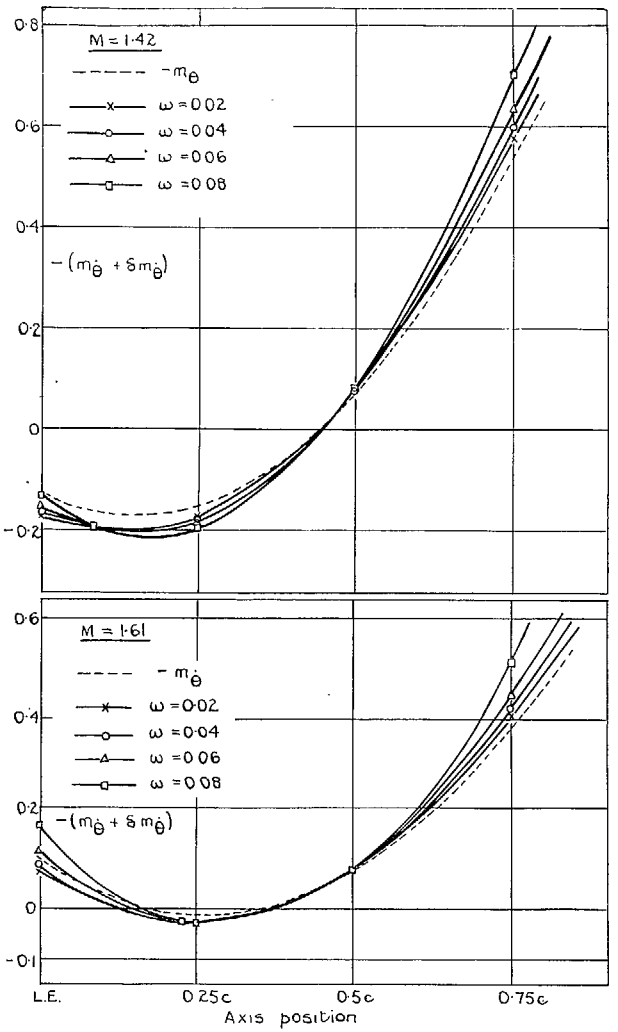

FIG. 48. Error in $-m_{\dot{\theta}}$ due to flexure—$7\frac{1}{2}$ per cent biconvex model.

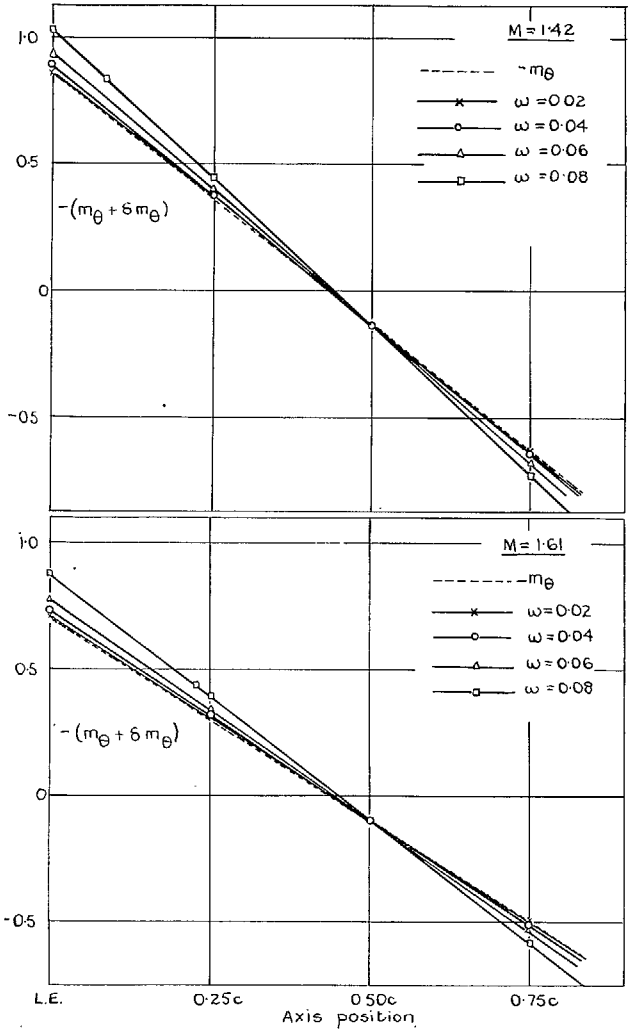

FIG. 49. Error in $-m_{\theta}$ due to flexure—$7\frac{1}{2}$ per cent biconvex model.

(83827) Wt. 67/1876 3/62 Hw.

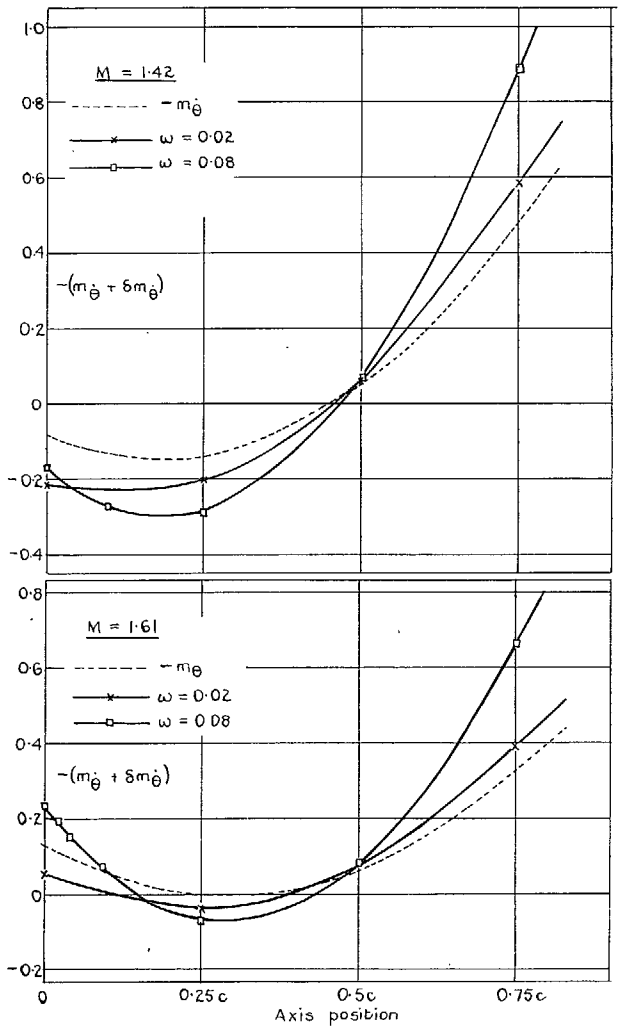

FIG. 50. Error in $-m_{\dot\theta}$ due to flexure—5 per cent biconvex model.

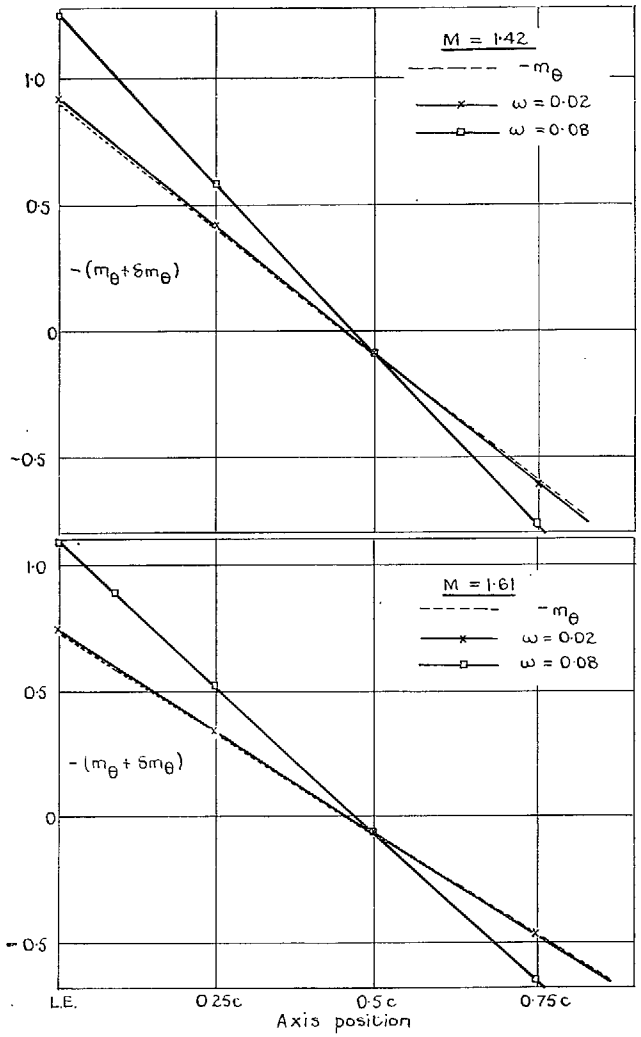

FIG. 51. Error in $-m_\theta$ due to flexure—5 per cent biconvex model.

Publications of the Aeronautical Research Council

ANNUAL TECHNICAL REPORTS OF THE AERONAUTICAL RESEARCH COUNCIL (BOUND VOLUMES)

1941 Aero and Hydrodynamics, Aerofoils, Airscrews, Engines, Flutter, Stability and Control, Structures. 63*s.* (post 2*s.* 3*d.*)

1942 Vol. I. Aero and Hydrodynamics, Aerofoils, Airscrews, Engines. 75*s.* (post 2*s.* 3*d.*)
Vol. II. Noise, Parachutes, Stability and Control, Structures, Vibration, Wind Tunnels. 47*s.* 6*d.* (post 1*s.* 9*d.*)

1943 Vol. I. Aerodynamics, Aerofoils, Airscrews. 80*s.* (post 2*s.*)
Vol. II. Engines, Flutter, Materials, Parachutes, Performance, Stability and Control, Structures. 90*s.* (post 2*s.* 3*d.*)

1944 Vol. I. Aero and Hydrodynamics, Aerofoils, Aircraft, Airscrews, Controls. 84*s.* (post 2*s.* 6*d.*)
Vol. II. Flutter and Vibration, Materials, Miscellaneous, Navigation, Parachutes, Performance, Plates and Panels, Stability, Structures, Test Equipment, Wind Tunnels. 84*s.* (post 2*s.* 6*d.*)

1945 Vol. I. Aero and Hydrodynamics, Aerofoils. 130*s.* (post 3*s.*)
Vol. II. Aircraft, Airscrews, Controls. 130*s.* (post 3*s.*)
Vol. III. Flutter and Vibration, Instruments, Miscellaneous, Parachutes, Plates and Panels, Propulsion. 130*s.* (post 2*s.* 9*d.*)
Vol. IV. Stability, Structures, Wind Tunnels, Wind Tunnel Technique. 130*s.* (post 2*s.* 9*d.*)

1946 Vol. I. Accidents, Aerodynamics, Aerofoils and Hydrofoils. 168*s.* (post 3*s.* 3*d.*)
Vol. II. Airscrews, Cabin Cooling, Chemical Hazards, Controls, Flames, Flutter, Helicopters, Instruments and Instrumentation, Interference, Jets, Miscellaneous, Parachutes. 168*s.* (post 2*s.* 9*d.*)
Vol. III. Performance, Propulsion, Seaplanes, Stability, Structures, Wind Tunnels. 168*s.* (post 3*s.*)

1947 Vol. I. Aerodynamics, Aerofoils, Aircraft. 168*s.* (post 3*s.* 3*d.*)
Vol. II. Airscrews and Rotors, Controls, Flutter, Materials, Miscellaneous, Parachutes, Propulsion, Seaplanes, Stability, Structures, Take-off and Landing. 168*s.* (post 3*s.* 3*d.*)

Special Volumes

Vol. I. Aero and Hydrodynamics, Aerofoils, Controls, Flutter, Kites, Parachutes, Performance, Propulsion, Stability. 126*s.* (post 2*s.* 6*d.*)

Vol. II. Aero and Hydrodynamics, Aerofoils, Airscrews, Controls, Flutter, Materials, Miscellaneous, Parachutes, Propulsion, Stability, Structures. 147*s.* (post 2*s.* 6*d.*)

Vol. III. Aero and Hydrodynamics, Aerofoils, Airscrews, Controls, Flutter, Kites, Miscellaneous, Parachutes, Propulsion, Seaplanes, Stability, Structures, Test Equipment. 189*s.* (post 3*s.* 3*d.*)

Reviews of the Aeronautical Research Council

1939–48 3*s.* (post 5*d.*) 1949–54 5*s.* (post 5*d.*)

Index to all Reports and Memoranda published in the Annual Technical Reports

1909–1947 R. & M. 2600 6*s.* (post 2*d.*)

Indexes to the Reports and Memoranda of the Aeronautical Research Council

Between Nos. 2351–2449	R. & M. No. 2450	2*s.* (post 2*d.*)
Between Nos. 2451–2549	R. & M. No. 2550	2*s.* 6*d.* (post 2*d.*)
Between Nos. 2551–2649	R. & M. No. 2650	2*s.* 6*d.* (post 2*d.*)
Between Nos. 2651–2749	R. & M. No. 2750	2*s.* 6*d.* (post 2*d.*)
Between Nos. 2751–2849	R. & M. No. 2850	2*s.* 6*d.* (post 2*d.*)
Between Nos. 2851–2949	R. & M. No. 2950	3*s.* (post 2*d.*)
Between Nos. 2951–3049	R. & M. No. 3050	3*s.* 6*d.* (post 2*d.*)

HER MAJESTY'S STATIONERY OFFICE

from the addresses overleaf

Printed and published by
HER MAJESTY'S STATIONERY OFFICE

To be purchased from
York House, Kingsway, London W.C.2
423 Oxford Street, London W.1
13A Castle Street, Edinburgh 2
109 St. Mary Street, Cardiff
39 King Street, Manchester 2
50 Fairfax Street, Bristol 1
35 Smallbrook, Ringway, Birmingham 5
80 Chichester Street, Belfast 1
or through any bookseller

Printed in England

S.O. Code No. 23-3257